

Final Report for award number NNX14AT50G

Dates covered by this report: 09/19/2014 to 03/31/2019

Proposal Title: Deep mapping of small solar system bodies with galactic cosmic ray secondary particle showers

Principal Investigator: Thomas H. Prettyman

Institution/address: Planetary Science Institute  
1700 E. Fort Lowell Road, Suite 106  
Tucson, AZ 85719

Email: prettyman@psi.edu

# Deep mapping of small solar system bodies with galactic cosmic ray secondary particle showers

T. H. Prettyman,<sup>1</sup> A. Empl,<sup>2</sup> L. S. Pinsky,<sup>2</sup> M. V. Sykes<sup>1</sup>, and M. C. Nolan<sup>3</sup>

<sup>1</sup>Planetary Science Institute, Tucson AZ

<sup>2</sup>University of Houston, Houston TX

<sup>3</sup>University of Arizona, Tucson AZ

Grant #NNX14AT50G

NASA Innovative Advanced Concepts  
Space Technology Mission Directorate

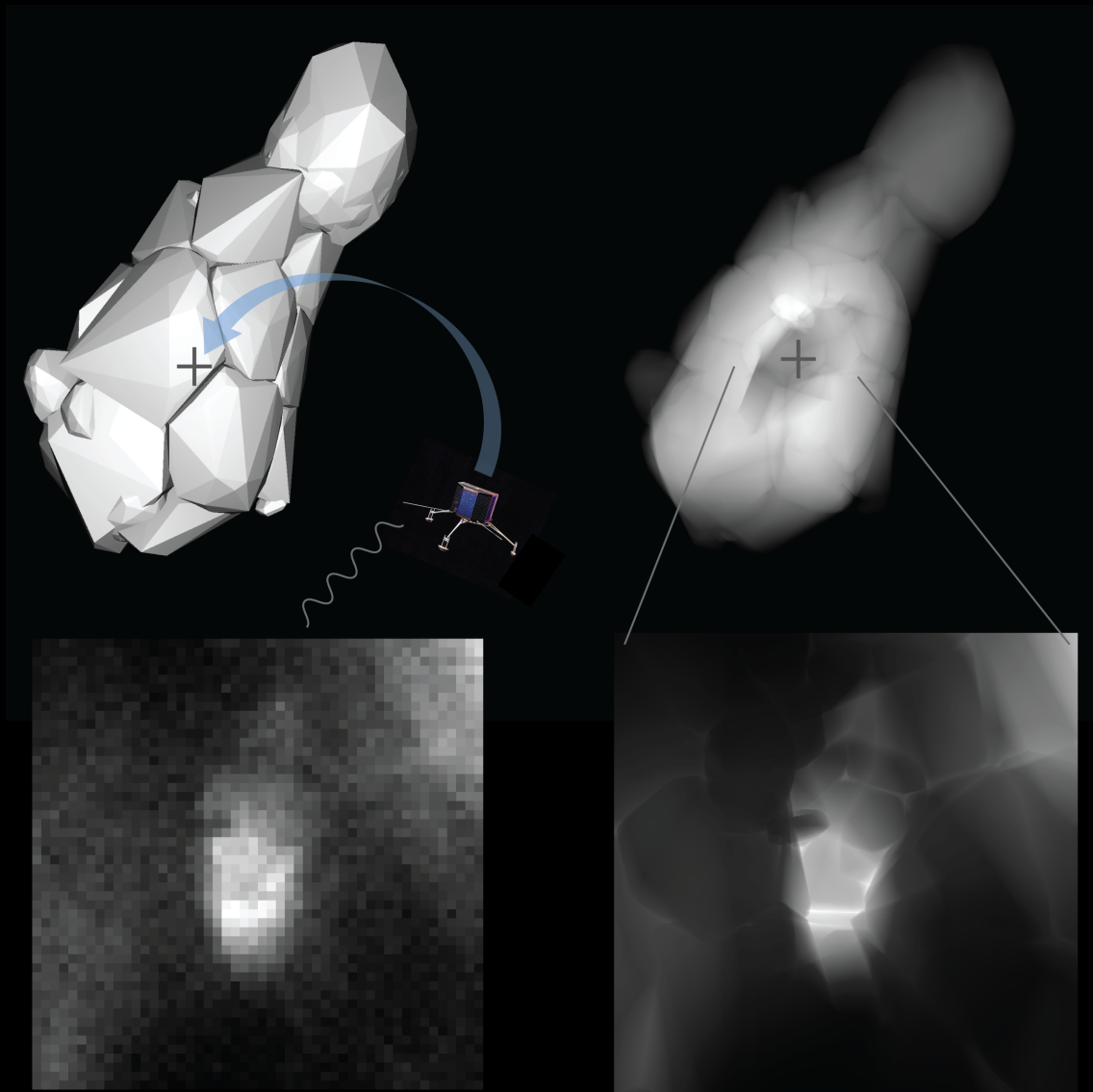


## Table of Contents

Summary of originally proposed research .....	4
Background: A brief history of muography.....	5
Introduction.....	7
Significance of small body interiors .....	8
Mapping small body interiors – Some alternatives.....	17
Muography of asteroids and comets .....	18
Radar constraints on regolith density.....	27
Use of FLUKA for GCR simulations .....	28
Detector simulations .....	33
Preliminary detector design .....	34
Detector performance.....	37
Mission concepts.....	41
Spin-offs.....	42
Conclusions and Next Steps.....	43
Acknowledgements.....	44
References.....	45

## Summary of originally proposed research

We will investigate the use of galactic cosmic ray (GCR) secondary particles to probe the deep interiors of small solar system bodies (SSBs), including comets, asteroids, and geologic structures on the surfaces of airless bodies. Applications include solar system science, planetary defense, and resource utilization. Our Phase I study demonstrated that muons, the long-range charged component of GCR showers, can penetrate SSBs up to a km in diameter, providing information on their interior structure. Muons produced in Earth's atmosphere have been applied to image the interior of large objects for science and engineering. In Phase I, we found that the production of muons in the solid surfaces of airless bodies is much smaller than in Earth's atmosphere. Nevertheless, the flux of transmitted muons is sufficient to detect inclusions within an asteroid or comet in a reasonable amount of time, ranging from hours to weeks, depending on the size of the SSB and the density contrast, position and size of the inclusion. For asteroids and comets, large density variations (e.g., porous soil or ice versus solid rock) are relatively easy to detect. The intrinsic spatial resolution of muon radiography ("muography") is on the scale of a few meters. The spatial resolution that can be achieved in practice depends on signal intensity and integration time (counting statistics), the angular resolution of the muon tracker (hodoscope) and details of data reduction and analysis methodology.

Our Phase II project will assess remaining unknowns for the application of muography to determining the interior structure of SSBs, assess risks for implementation, and provide a roadmap for development of SSB muography beyond the NIAC program. To achieve our objectives, we will focus on four interrelated tasks:

Task1) **Signal and background characterization:** Characterize the production and transmission of muons and secondary particle backgrounds made by cosmic ray showers in SSBs; and near-surface features from radiographic and tomographic data;

Task2) **Imaging studies:** Develop methods to determine the density structure of SSB interiors and near-surface features from radiographic and tomographic data;

Task3) **Instrument design:** Using simulations and bench-top laboratory experiments, investigate specific concepts for the design of compact hodoscopes and components;

Task4) **Synthesis:** Combine the results of the first three tasks to determine the range of applicability of the method, identify the steps needed for maturation of the concept, and explore concepts for a pilot muography mission.

## Background: A brief history of muography

The application of cosmic ray secondary particle showers to image large structures on the surface of the Earth was pioneered by Luis Alvarez, who used muons to explore the structure of the Chephren's Second Pyramid (Alvarez et al., 1970). Energetic muons, highly-penetrating, charged particles, are produced in abundance by galactic cosmic ray interactions in the upper atmosphere. On the order of 10,000 muons per square meter per minute reach the surface of the Earth, providing an intense source that can be used for radiography. The muon imager, a spark chamber with precise directional sensitivity, was situated within an interior chamber near the middle of the base of the pyramid. Devices that determine the direction of energetic ionizing particles, such as atmospheric muons, are known as hodoscopes. The imaging method is analogous to X-ray radiography.

Variations in the attenuation of muons through the limestone rock that made up the pyramid were compared to models that treated the pyramid's established geometry. These comparisons revealed known structural features, such as the edges of the pyramid and its limestone casing cap. No additional chambers were detected, consistent with the simplification of pyramid architecture following the construction of the Great Pyramid of Cheops. Nevertheless, the experiments convincingly demonstrated that muons could be used to radiograph the interior of large structures (about 100 m scale). Thus began the era of muon radiography, which has been dubbed "muography" in recent times.

Nearly 50 years later, Morishima et al. (2017) mapped the interior of the Great Pyramid using nuclear emulsion film along with scintillator- and gas-hodoscopes. The emulsion film and scintillator hodoscopes were initially positioned in the Queen's chamber inside the pyramid (Fig. 1a). As with the Alvarez et al. study, the data revealed known structures, including the King's chamber and Grand Gallery; however, the radiographs also show a ~30-m scale region with low muon attenuation ("New Void" in Fig. 1b). This region was subsequently detected in muon radiographs acquired outside the pyramid using gas hodoscopes. The credibility of the study was strengthened by the use of multiple detector technologies. This was the first discovery of an interior void within an Ancient Egyptian pyramid in over 100 years.

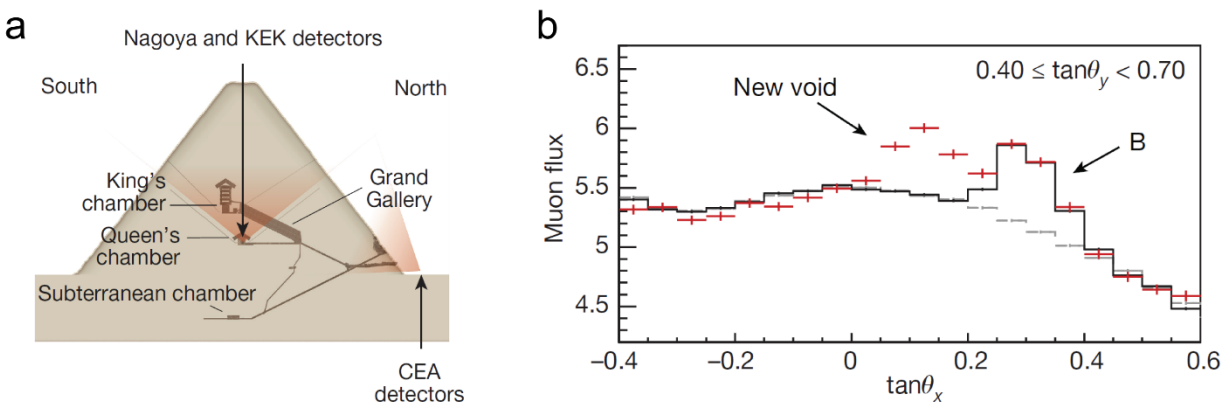


**Figure 1.** a) A cross section of the Great Pyramid shows the placement of muon imagers inside the King's chamber (Nagoya/KEK) and outside the pyramid (CEA). b) Comparison between modeled muon hits (black) and measurements (red) reveal a void in the pyramid. The figures are from Morishima et al. (2017).

In studies by Alvarez et al. and Morishima et al., the data were acquired over months, and — with the exception of the gas hodoscopes — using sensors with active areas greater than a square meter.

Prior to Alvarez et al.'s experiments, atmospheric muons were used to measure the thickness of rock overlying a subterranean region (George, 1955). Using a Geiger-counter telescope, George and his students measured the overburden within a tunnel at depths of about 70 m. Their results were consistent with drill core depths. Similarly, Tanaka (2015) mapped the overburden within peninsulas in Japan. In this case, a time-series of muon counts was acquired from a motor vehicle as it was driven through tunnels distributed throughout the peninsulas. The data were used to determine rock density and porosity, constraining aspects of regional geology. These studies were influential in our considering cave science as a possible application for muography. A subset of the NIAC deep mapping team and collaborators has been exploring the development of very compact and simple-to-operate overburden gauges that could be deployed in caves. This work is summarized later in the report.

An early application of muon radiography to geology was carried out by a group led by Tanaka (e.g. Tanaka et al., 2007). They imaged the density structure of a ~km scale volcano using a large-area (4000 cm<sup>2</sup>) emulsion cloud chamber. The horizontal flux of atmospheric muons was used to probe the base of the volcano. A couple of months of integration were required to achieve the desired measurement precision. The data when combined with topography revealed new aspects of the volcano's "plumbing," including the presence of a vent cap covering a permeable region through which lava could flow. This laid the groundwork for geologic studies that followed along with improvements in methods and instrumentation (Fig. 2). Studies included radiographic visualization of magma dynamics, volcanic degassing, and evolution of their interior structure (e.g. Tanaka Hiroyuki, 2019; Tanaka et al., 2014; Tanaka et al., 2009; Tioukov et al., 2019).

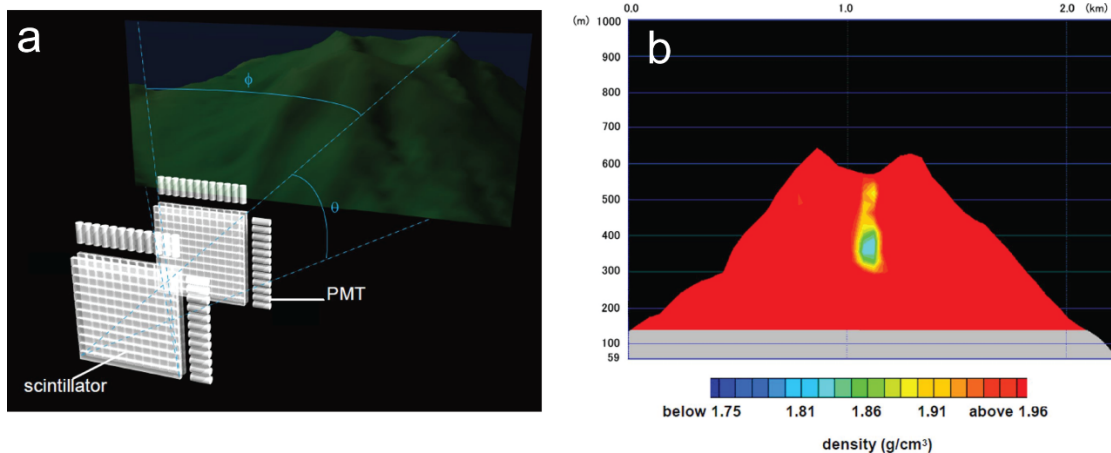


**Figure 2.** a) Diagram of a portable muon hodoscope consisting of two, position-sensitive scintillating layers read out by photomultiplier tubes (PMT). The active area was approximately 1 m<sup>2</sup>. b) The hodoscope was used to image the internal density structure of Mt. Iwodake, an active volcano on Satsuma-Iwojima island. Approximately a week of integration time was required. The figures are from Tanaka et al. (2009); (Tanaka et al., 2010).

## Introduction

Given the success of terrestrial applications of muography, it is natural to wonder whether these techniques could be applied in other planetary settings. As small solar system bodies are of increasing interest to NASA, we proposed to investigate the use of secondary particles produced by galactic cosmic ray showers to image the interior density structure of asteroids and comets. This work was supported by the NASA Innovative Advanced Concepts (NIAC) program. Our Phase I project defined the concept and identified some of the limitations (Prettyman et al., 2014). In Phase II, we further investigated the viability of the concept, including the identification of a feasible detection system, supported by simulations and laboratory experiments. Results of the Phase II effort are reported here.

The concept is sketched in Fig. 3, which illustrates production, transport, and detection of muons passing through a small near-Earth asteroid (NEA), modeled as 25143 Itokawa. High energy muons can penetrate the asteroid with negligible deflection from straight-line paths, which could enable radiography of the interior density structure. However, production of muons in solid materials is expected to be quite low compared to Earth's atmosphere. In addition, knowledge of surface density is required to separate muon production from attenuation. Finally, the detector (hodoscope) must be designed to reject secondary particle backgrounds, which could overwhelm the through-asteroid signal.

The report reviews the significance small body interiors and provides a description of the concept along with possible alternatives for deep mapping. Muon radiography is explored using asteroid models and a simple model of muon production and attenuation. End-to-end simulations of spherical bodies support the assessment of a feasible detection system capable of muon directional tracking and background rejection. Prospective missions and possible spin-off applications are described.

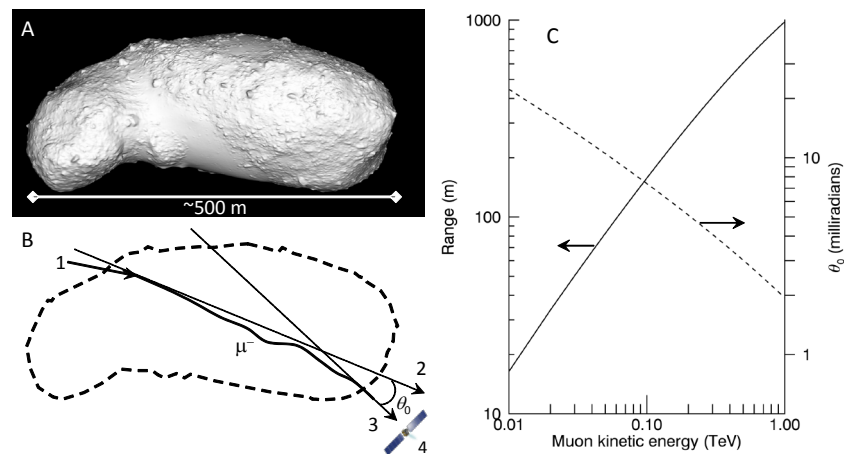


**Figure 3.** Deep mapping concept: A) Orthographic projection of NEA Itokawa showing the surface texture, which includes large boulders and fine grained materials. B) Trajectory of a muon through the asteroid: 1) Production of a muon within the outermost few meters of the asteroid by the interaction of a galactic cosmic ray; 2) path of the muon through the asteroid, illustrating its 3) deflection by scattering processes; and 4) detection of the muon by an orbiting imaging system. C) Muon range and cumulative deflection  $\theta_0$  as a function of the initial kinetic energy of the muon.

## Significance of small body interiors

Knowledge of the interior structures of small bodies in the solar system is critical to understanding their accretion, collisional history and evolution, thereby providing important information on the conditions of the early solar system under which they formed and how that environment evolved. Small bodies are also targets for future human exploration. So, their interior structures are important to understanding the mechanical properties of these targets, their stability, and their potential operational hazard. Small bodies also offer potential materials that would be valuable for in-situ resource utilization, to underpin self-sustainable infrastructure supporting expanding human activities in space as well as resources to support economic activity including robotic satellite maintenance and refueling. Any effort to mine asteroid material in-situ will need to accommodate the interior properties of a target object. Understanding the interior structures of small bodies is also necessary input for the assessment of mitigation strategies in planetary defense.

### Expectations

Small bodies, particularly in the inner solar system, are expected to have internal structures ranging from coherent and monolithic to some configuration of rubble pile (e.g. Davis et al., 1979). What do we expect the interior of a rubble pile to look like?

Rubble piles are formed when an object is catastrophically shattered, but without enough energy to disperse all of the fragments away from each other. Some remainder, under mutual gravitational influence, pull back together into a pile of aggregate. Now, if you have a box of rocks (i.e., asteroid fragments) of a wide range of sizes and you give it some good shakes, you can fill almost all of the interior pores with the result that the bulk density of the aggregate is near that of the constituent rock density (assuming a common rock density). Assuming coherent rock components, decreasing an asteroid's bulk density and increasing its porosity would require a size sorting of the fragments from which the asteroid accreted.

Laboratory impact experiments show that smaller fragments are ejected with greater velocities than larger fragments (e.g. Nakamura & Fujiwara, 1991). So, the size-distribution of re-accreted fragments would depend upon time of accretion and the level of size-sorting achieved by then.

Packing equal sized spheres in an arrangement that is stable against compression can result in a range of void fractions from 26% (Gauss, 1831) to 51% (Torquato & Stillinger, 2007). In the case of accretion in a low gravity environment, friction and other factors might allow for unstable configurations of greater void fractions.

So, rubble piles, as re-accretions, can have a range of porosities corresponding to (for low porosities) bulk densities near that of the constituent rocks (for close-packed rocks spanning a large size distribution) up to (for high porosities) much lower bulk densities created by a narrower range of rock sizes where frictional forces would allow for unstable configurations to be created.

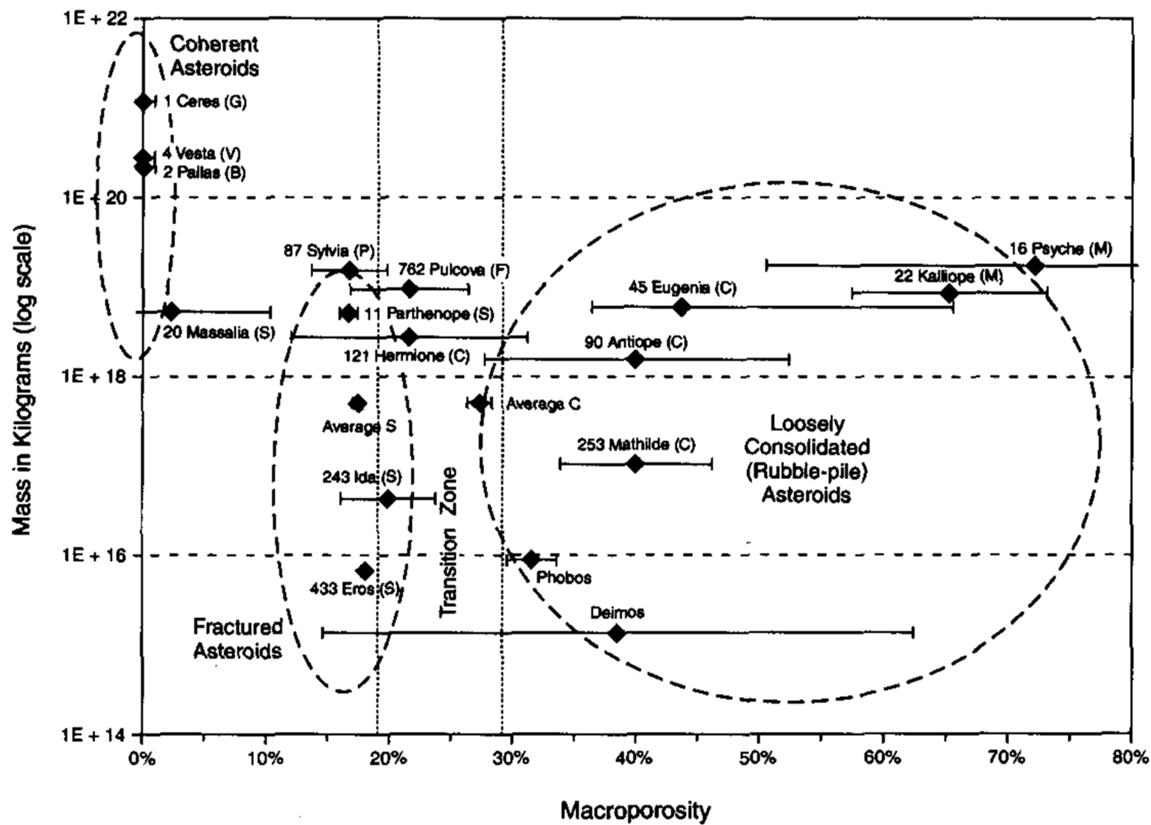


**Figure 4.** Asteroid macroporosity estimated by subtracting the average porosity of the asteroid’s meteorite analog from the bulk porosity determined from mass and volume determinations. Since microporosity does not seriously affect the structural integrity of asteroids, this is thought to be a direct estimate of the large-scale fractures and voids that determine the asteroids internal structure. Figure and caption from Britt et al. (2002).

### What Do We Know About Small Body Interiors?

In the absence of any direct knowledge of asteroid interiors, we need to infer their structure primarily from estimates of bulk density and comparison with analog meteorite densities.

The results shown in Fig. 4 align with our expectations based on our understanding of the composition of these bodies, their mechanical properties, and the collisional and accretion processes to which they are subject. With large objects (e.g., Ceres and Vesta), there is sufficient heat to cause differentiation of the interior. Also, gravitational forces are sufficient to overcome material strength in the interior. Some smaller objects will be impacted. If impacts are insufficient to catastrophically disrupt an object, it can be partially fragmented, leaving voids by fractures. An object can be disrupted and re-accrete, and if each re-accreting fragment is strong enough to resist gravitational crushing, then you can have more significant voids.

It must be acknowledged, however, that “void” may not be a vacuum-filled space devoid of material. The interior of a small body may contain regions of distinguishably higher and lower densities, so “voids” would refer to the lower density regions. One might think of denser components smashing together to form a larger object consisting of denser fragments and loose aggregate filling or partially filling the spaces between them.

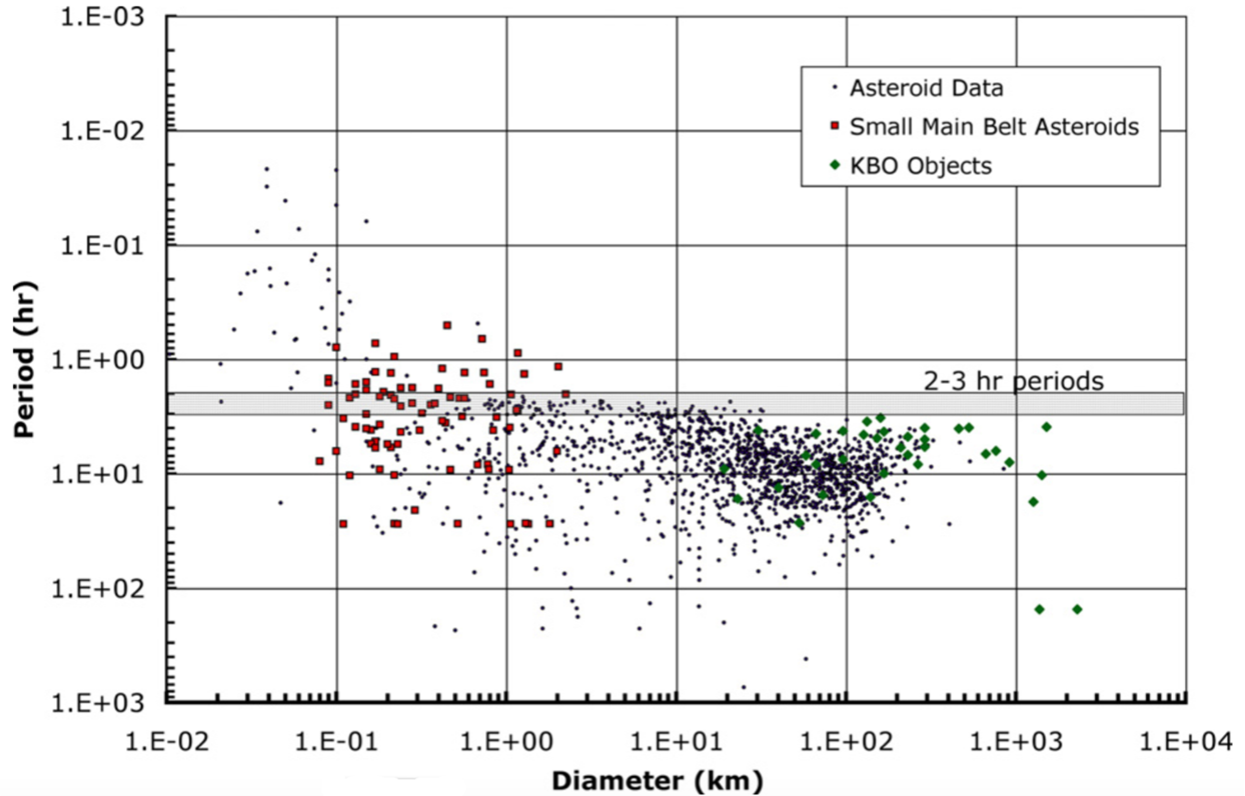


**Figure 5.** The spins of approximately 1500 asteroids as a function of their diameter. The dots on the left with a period above about 1 h are the ‘fast-spinning asteroids,’ all NEA’s. The set with square symbols are main belt asteroids. And about 20 KBO’s are shown at the right. All of the bodies with diameter >3 km have periods less than 2.30 h. The broad horizontal band labeled “2–3 h periods” is the theoretical range of upper limits for materials without cohesive or tensile strength. Figure and caption from Holsapple (2007).

There is evidence that some small asteroids may be monolithic. In Fig. 5, such internal strength is inferred from their rapid rotation rates, which would nominally break up a rubble pile of no strength held together by self-gravity. In this case, one would expect no interior cracks or voids of significance. However, Van der Waals forces between constituent grains may give small rubble pile asteroids a small but nonzero cohesive strength, preventing the breakup of small, rapidly rotating asteroids (Sánchez & Scheeres, 2014; Scheeres et al., 2010). Such forces could be another factor promoting increased macroporosity (void fraction) in asteroids of km diameter and less (that are not rapidly rotating!).

The structure of Jupiter family comet interiors may arise from a similar but distinctive range of processes compared to main belt asteroids. Jupiter family comets originate in the Kuiper belt, where orbital velocities and impact velocities are much lower than in the inner solar system. The New Horizons flyby of the KBO Ultima Thule (Fig. 6) reveals the consequence of such a low-energy environment on accretion.



**Figure 6.** Ultima Thule, observed by the NASA New Horizons mission (Courtesy, NASA/JHU APL/SWRI/NOAO).

Ultima Thule is a contact binary, formed by a very low velocity collision of two low-strength objects. This is supported by the bright ring of small-particle materials at the “neck” and no evidence of target or impactor fragmentation as a consequence of the collision. The morphology of each of the contact components is distinctly “lumpy”, giving the appearance of very low velocity accretion of low-strength bodies on the order of a few kilometers in diameter and smaller. With the original shapes of the contact binary components so intact, it is not hard to imagine that the interiors of the components might preserve actual voids between the constituent objects forming them.

In summary, there is good reason to think that interiors of small bodies are highly varied. Even objects of the same size and composition could have very different interior structures as a consequence of the details of their collisional history that that of their parent bodies. A differentiated, Vesta-like protoplanet with a basaltic crust that was subsequently disrupted could form child-asteroids that include solid, monolithic objects; objects dominated by the aggregation of a number of large, intact fragments; rubble piles of well-pulverized material; or a combination of large, solid fragments and small rubble. It is not possible to distinguish among these different interior structures by distant, remote observations. It can only be probed in close proximity to the object.

### **Identifying Targets**

The Near-Earth Object (NEO) population presents a unique opportunity to study objects which have formed throughout the solar system without having to travel to the more distant source locations. Bottke et al. (2002) reports “~61% of the NEO population comes from the inner main

belt ( $a < 2.5$  AU), ~24% comes from the central main belt ( $2.5 < a < 2.8$  AU), ~8% comes from the outer main belt ( $a > 2.8$  AU), and ~6% comes from the Jupiter-family comet region” (Fig. 7). As a consequence, NEOs are highly diverse physically and compositionally.

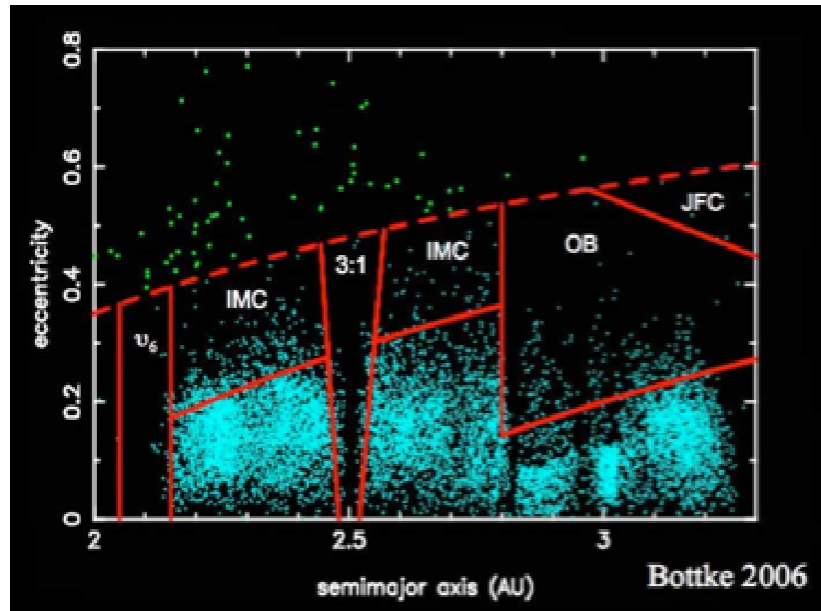


**Figure 7.** NEOs come from regions throughout the main asteroid belt and Jupiter family comets, which in turn derive from the Kuiper Belt. The chart is based on Morbidelli et al. (2003).

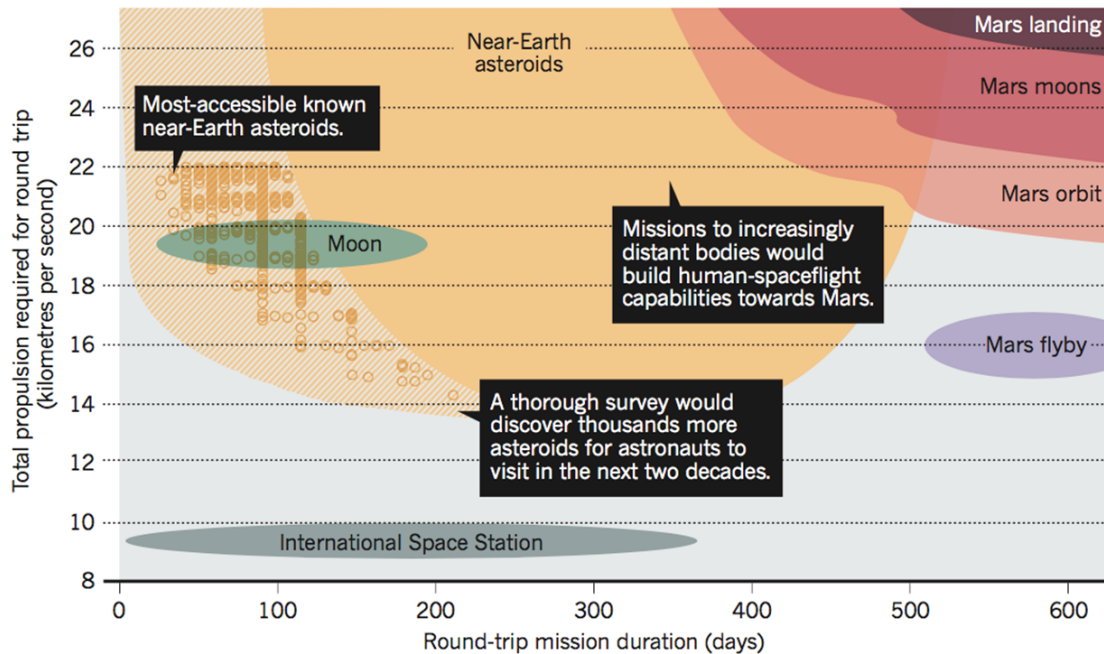


**Figure 8.** Less than 1% of the most-accessible asteroids are currently known (yellow circles), but a dedicated survey (filling in the yellow-hatched region) would reveal abundant near-Earth asteroid mission opportunities that would require less fuel and less mission times than a mission to lunar orbit (Binzel, 2014).

Understanding the interior structure of a diverse population of small bodies requires a large number of appropriately instrumented rendezvous missions to sample that diversity. NEOs represent not only a diverse source population, but has the dynamical accessibility required to target a large number of missions. This is illustrated in Fig. 8, in which it is seen that NEOs can require less fuel and quicker mission times than a mission to lunar orbit. The one drawback is that NASA has not undertaken the space-based infrared survey mission required to maximize the population of potential mission targets while at the same time satisfying the Congressional requirement for discovering potentially hazardous NEOs with diameters exceeding 140m (Stokes et al., 2017).

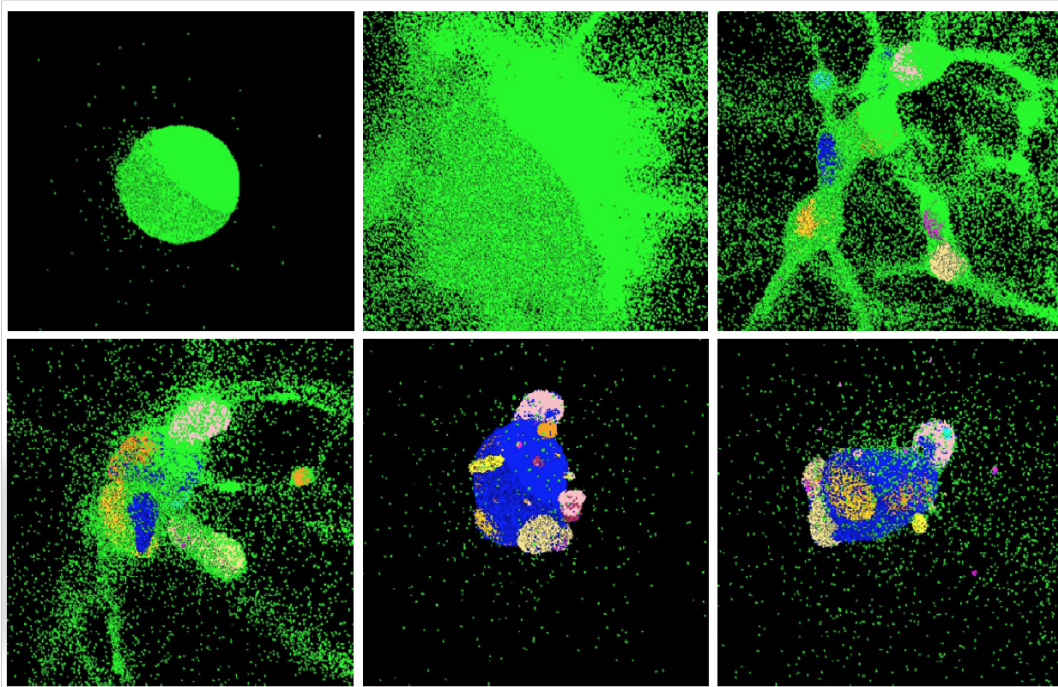


**Figure 9.** Forming near-Earth asteroid 25143 Itokawa by re-accumulating the fragments from the catastrophic disruption of a 25 km asteroid (Michel & Richardson, 2013).

Jupiter family comets that end up in the NEO population will necessarily have experienced a much greater collisional and thermal environment than their source region in the Kuiper Belt. Consequently, their interior structure is likely to have evolved. In addition to pristine KBOs, the small satellite population of the outer planets, some of which were captured from scattered objects closer to the Sun as well as objects evolving in from the Kuiper Belt, are not represented in the NEO population. The study of their interior structure would require more expensive missions to these more distant reaches. The study of very accessible targets shown in Fig. 8 could be accommodated by small, sub-Discovery class missions, allowing for large numbers of such missions. Exploring small satellites in the Outer Solar System could be accommodated by piggy-backing small spacecraft onto large missions sent to study gas giants, Pluto and other icy dwarf planet systems in the Kuiper Belt.

### A Diversity Twist

No small asteroids are “primitive.” They have all been processed by collisions (Fig. 9). They have fragmented and re-accreted, forming “rubble piles.” It is easy to think of them as being

compositionally homogeneous, determinable by remote spectroscopic observations, but this may be very misleading.

In 2008, a small (4 m diameter) asteroid was identified by the Catalina Sky Survey 19 hours before it entered the Earth's atmosphere (McGaha et al., 2008; Shaddad et al., 2010). It exploded over Sudan near a train station called Almahata Sitta. In the case of the Almahata Sitta precursor, 99.9% of the mass was lost. "Based on MeteorSat observations of the atmospheric entry of 2008 TC<sub>3</sub>, Borovička and Charvát (2009) estimated that the nonsublimated dust particles in these clouds were micron-sized, suggesting that the bulk of the asteroid was extremely fine-grained. In addition, estimates of the bulk density of the asteroid from abundances of cosmogenic radionuclides in the meteorites are in the range 1.2–1.6 g cm<sup>3</sup>, which is significantly lower than densities of any of the meteorites and indicates a bulk porosity of 50 +/- 7% (Welten et al., 2010). Thus, we infer that 2008 TC<sub>3</sub> consisted mostly of highly porous, weakly consolidated matrix material, with only a small fraction of isolated, larger sized fragments of denser, well-consolidated rocks that became the fallen meteorites" (Goodrich et al., 2015).

The scattered meteorites were compositionally diverse. They were ~69% ureilites (ultramafic achondrites, derived from a differentiated parent body) and the other 31% are various types of chondrites, supposedly primitive meteorites, from un-melted parent bodies (Goodrich et al., 2015). So, the components of the Almahata Sitta meteorite originated in significantly different locations under different conditions. Meteorite bulk densities in general span 2-3.5 g/cm<sup>3</sup> for carbonaceous and ordinary chondrites to 7-8 g/cm<sup>3</sup> for irons. The extent to which compositional inhomogeneity is common, inferring interior structures from inferred "bulk" properties including spectral measures is yet more difficult.



**Figure 10.** 67P/Churyumov-Gerasimenko. Target of the Rosetta spacecraft.

### **What Might Muon Tomography Reveal About the Interiors of Comets?**

Comets are mostly low-density rock by mass, with a dust/gas (D/G) mass ratio of ~3 (Sykes & Walker, 1992). Most of these particles may be "trail" particles most consistent with large, dark, low-density spheres that are rapidly rotating and randomly oriented (Sykes et al., 2004).

Fairy-castle interplanetary dust particles (10s of mm) associated with comets and dust trail particles (mm-cm or larger) suggest that comet material accretes at low density (0.6-1 g/cm<sup>3</sup> and

possibly quite lower). The loss of interstitial water from this material could diminish interior densities in some areas or result in cavity formation on the surface. Low bulk densities do not mandate the existence of substantial voids in the interiors of comets.

Consider 67P/Churyumov-Gerasimenko (Fig. 7). Assume:

$$\begin{aligned}\rho_{\text{dust}} &= 2.1 \text{ g/cm}^3 \text{ (CI)} \\ \rho_{\text{ice}} &= 1 \text{ g/cm}^3 \text{ (water ice)} \\ D/G &\sim 3\end{aligned}$$

$$\begin{aligned}V_{\text{tot}} &= 21.4 \text{ km}^3 \\ M_{\text{tot}} &= 10^{13} \text{ kg} \\ \rho_{\text{tot}} &= 0.47 \text{ g/cm}^3\end{aligned}$$

$$\begin{aligned}V_{\text{dust}} \rho_{\text{dust}} + V_{\text{ice}} \rho_{\text{ice}} &= M_{\text{tot}} \\ V_{\text{dust}} \rho_{\text{dust}} / (V_{\text{ice}} \rho_{\text{ice}}) &= 3 \\ V_{\text{dust}} + V_{\text{ice}} + V_{\text{void}} &= V_{\text{tot}}\end{aligned}$$

Then,

$$\text{Porosity} = V_{\text{void}} / V_{\text{tot}} = 70\% \text{ (or lower if dust a porous aggregate)}$$

On the other hand, assuming the basic building block of comets are low-density assemblages of CI-type material, various mechanical processes would work to locally compress this material. This would include massive reconfiguration of the comet's material, as occurs with 67P/Churyumov-Gerasimenko (Fig. 10). Pressure of local outgassing and material collapse could also result in material compression, along with impacts (which may also trigger the previous two processes).

Density discontinuities between compressed and uncompressed comet material, could perhaps be manifested as sheets of high-density within low-density material, e.g., 0.5 g/cm<sup>3</sup> (uncompressed) and 2 g/cm<sup>3</sup> (compressed).

### **What Might Muon Tomography Reveal of Asteroid Interiors?**

Voids would be present on the order of the size of the constituent fragments comprising the asteroid – possibly larger depending upon the role of friction and van der Waals forces.

Density contrasts: ~3 g/cm<sup>3</sup> (component rock) vs, 0 g/cm<sup>3</sup> (voids)

Alternatively, if asteroids have little voids, but low-density fill instead, the density contrast would be lower.

Density contrasts: ~3 g/cm<sup>3</sup> (compact rock) vs. ~1 g/cm<sup>3</sup> (low-density fill)

## **Value to Science**

Interiors are the last great unknowns of small body interiors, providing critical constraints on their formation, evolution, and the collisional conditions in different regions of the solar system.

## **Value to Human Exploration**

The proposed Asteroid Retrieval Mission (ARM) envisioned the capture of a small (~7m) asteroid in a large bag and returning it to retrograde lunar orbit using a high-power solar electric propulsion system (e.g. Mazanek et al., 2013). Such a target was thought more likely to be coherent or monolithic. The possibility of it being a rapid rotator was a concern along with uncertainty of size and density at the time of mission launch. Retrieving a boulder from a small NEA was thought to offer greater knowledge a priori about its characteristics as inferred from its parent body. “Moonlets” were also contemplated, but thought likely to be rubble piles. Basically, there was no basis for assuming any particular structure of these objects. ARM could have approached what it thought might be a monolithic object, only to discover it is a dust-bank held together by van der Waals forces, potentially disintegrating at first contact. This is the same risk posed to humans – potential unstable interior structures that could reconfigure with contact at some level, thus posing a risk to astronauts.

## **Value to ISRU**

The availability and cost of developing processes for extracting and transporting near-Earth asteroid resources for propulsion fuel, life support, and radiation shielding may be the ultimate limit for establishing a sustainable, expanding human population and economy beyond Earth. Near-Earth asteroid resources may be essential to easy access of the lunar surface and the practical access of the surface of Mars. This will likely require the processing of large numbers of NEOs and knowing the structure and mechanical properties of the interior will be needed to develop automated resource reclamation facilities.

## **Value to Planetary Defense**

Practical methods of modifying the orbit of an asteroid found to be on a collision course with the Earth will depend primarily on the time to impact (short times minimize options). A popular method being tested today is the kinetic impactor. The ability to predict the efficiency of momentum transfer is a large unknown that requires, in part, a knowledge of the interior of the object.

## Mapping small body interiors – Some alternatives

Several methods have been proposed for mapping the interior structure of small bodies. These include radar, gravimetry, seismic imaging, and muography (this study). Table 1 indicates the physical parameter that each of these methods is sensitive to along with the potential object size and resolution limit along with perceived limitations.

Small-body densities can be addressed in several ways using radar observations, though there are a number of complications that make it more complicated and harder to interpret than, for example, the SHARAD measurements of the Martian surface (e.g. Phillips et al., 2008). The CONSERT instrument on ROSETTA was intended to perform radar transmission tomography using a transmitter on Philae (Ciarletti et al., 2015; Kofman et al., 2015). Radar measurements indicated 67P/Churyumov-Gerasimenko is homogeneous on scales of several meters and provided constraints on the volumetric dust/ice ratio and porosity. Gravity measurements confirmed the high porosity of the comet and the absence of large voids (Pätzold et al., 2016). Other in-situ radar measurements of asteroid and comets have been proposed as well (e.g. Sava & Asphaug, 2018).

The use of gravity gradiometers to determine the internal mass distribution of small bodies has been considered since the 70s. Recently, a NIAC team completed the assessment of swarm gravimetry, concluding that this method could significantly improve the accuracy and sensitivity of the mass of small bodies compared to Doppler-only methods (Atchison, J., NIAC Phase II report, 2017). Surface observations can provide clues to how seismic energy propagates through asteroid interiors (e.g. Thomas & Robinson, 2005) and active methods to probe the interior structure of small bodies have been proposed (e.g. Plescia, J., NIAC Phase I report, 2016).

Muography is sensitive to the density of materials within the asteroid or comet. The density distribution could be determined on very fine scales; although, long integration times would be required. In practice, multiple observations will be required to reliably determine properties of the deep interior, including observations of surface structure/properties and spin/orbit dynamical effects.

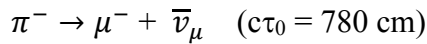
Table 1. Comparison of different methods that have been considered for mapping the interior structure of small solar system bodies.

Method	Physical Parameter	Object size or depth	Resolution limit	Issues
<b>Radar</b>	Dielectric constant, conductivity	Meters to kilometers, dependent on wavelength	meters	Contrast detection, ambiguous
<b>Gravimetry &amp; Radio Science</b>	Gravity field	Whole-body, regional mass anomaly	?	Model based
<b>Seismic</b>	Seismic velocity, density	kilometers	Thin structures challenging	Contrast detection, ambiguous
<b>Muography</b>	Density	< a few hundred meters	meters	Long integration times

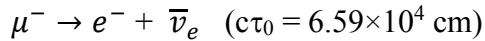
## Muography of asteroids and comets

The surfaces of airless bodies are exposed to a steady flux of galactic cosmic rays (GCRs). These are mostly ions originating from distant sources outside the solar system, including shell-type supernova remnants and active galactic nuclei. Near their source, they are accelerated to very high energies (e.g. by Fermi acceleration processes). Propagation occurs along interstellar field lines, which results in an isotropic distribution of particles. Their energy distribution follows a power law, consistent with the production of ions by Fermi acceleration processes. Their average kinetic energy is in the GeV range; although, particles with kinetic energy greater than  $10^{20}$  eV have been observed.

GCR primary and secondary ions can penetrate several meters into the regolith of airless bodies (asteroids and comets). Collisions between energetic ions and nuclei produce a spray of secondaries, which subsequently undergo further collisions, making a particle shower, consisting of hadrons (ions and mesons), leptons, and electromagnetic radiation (Fig. 11). The secondary particles include kaons and pions, which decay to produce muons and neutrinos, e.g.



where  $c\tau_0$  is the decay constant (see Gaisser, 1990). The muons decay with a mean lifetime of 2.2  $\mu\text{s}$ , e.g.



Time dilation extends the decay length of relativistic particles, such that muons produced in the Earth's upper atmosphere reach the surface in abundance (i.e. multiply the decay constant by  $\beta\gamma$  to get the decay length of a relativistic particle — where  $\beta$  is the velocity relative to the speed of light and  $\gamma$  is the Lorentz factor). In the upper atmosphere, a significant portion of mesons decay to muons before colliding with atmospheric nuclei; however, in a solid surface, collisional processes dominate. The destruction of mesons prior to decay results in a diminished flux of muons in solid surfaces compared to Earth's atmosphere.

In Phase I, an approximate scaling of muon production with density was derived using a semi-empirical cascade model popularized by Gaisser (1990), in which muon production was modeled as a balance between meson collisional losses and decay. The contribution to the vertical differential flux of muons at sea level (about 1000  $\text{g}/\text{cm}^2$  depth) for each meson meson ( $m = \pi, K, D, \dots$ ) has the following functional form:

$$\varphi_m(E) = aE^k \left[ \frac{A_m}{1 + B_m E/\varepsilon_m} \right] \quad \text{muons}/(\text{cm}^2 \text{ s sr GeV}) \quad \text{Eq. 1}$$

where  $E$  is muon energy (GeV). The term  $E^k$  is proportional to the flux of primary galactic cosmic ray nucleons.  $A_m$  is proportional to the spectrum-weighted moment of the nucleon-pion

cross section;  $B_m$  is a function of the ratio of meson to nucleon attenuation lengths. Both of these terms depend on the chemical composition of the medium. The term  $E/\varepsilon_m$  is the decay length of the meson ( $m$ ) with energy  $E$ , given by  $d_m = \rho \gamma (c \tau_0)_m$ , where  $\rho$  is density ( $\text{g/cm}^3$ ),  $\gamma$  is the Lorentz factor and  $c \tau_0$  is the meson's decay constant. The numerical values of the parameters were tabulated by Gaisser (1990).

In Phase II, the Monte Carlo code FLUKA was used to simulate the vertical flux of muons produced by the interaction of solid surfaces with densities of 0.5-, 1-, and 2- $\text{g/cm}^3$ , consistent with the range expected for asteroid regoliths. The composition was "standard rock," with  $Z=11$ ,  $A=22$ , approximately  $(\text{FeO})_{0.2}(\text{SiO}_2)_{0.8}$ . Muon production is primarily in the uppermost meter of the surfaces studied. The Gaisser cascade model compares favorably with the FLUKA calculations above 100 GeV. Both predict significantly lower fluxes in solid surfaces compared to Earth's atmosphere.

Combining the FLUKA calculations with the cascade model, the following scaling was found for the flux of muons produced in solid surfaces above 1 GeV:

$$\Phi(E_\mu > 1 \text{ GeV}) = 10^{-0.7 \log(\rho) - 3} \text{ muons / cm}^2 / \text{s} / \text{sr} \quad \text{Eq. 2}$$

This gives muon vertical flux of  $\sim 8 \times 10^{-4}$  muons/ $\text{cm}^2/\text{s}/\text{sr}$  in solid materials with a density of 2  $\text{g/cm}^3$ . This is an order of magnitude lower than the sea-level vertical flux of muons produced in Earth's atmosphere ( $7 \times 10^{-3}$  muons/ $\text{cm}^2/\text{s}/\text{sr}$ ). The production of muons decreases sharply with density. For example, the vertical flux for a solid, iron-nickel composition ( $\rho = 8 \text{ g/cm}^3$ ) would be  $\sim 2 \times 10^{-4}$  muons/ $\text{cm}^2/\text{s}/\text{sr}$ . The Phase I study showed that the makeup of the regolith does not significantly affect muon production. Note that the production of high-energy muons that can penetrate thick targets is unaffected by solar modulation of galactic cosmic rays. A steady flux of muons is available for radiography.

Muons are leptons with a rest mass roughly 200 times that of an electron. Energy loss is primarily by ionization and radiation (Groom et al., 2001). Because they are massive, they are not significantly deflected by collisions, such that they travel in approximately straight lines over very long distances (for example, see Fig. 1). This makes muons an ideal particle for probing the structure of large objects on fine scales. Stopping power does not depend strongly on composition (e.g. Fig. 13), which means that measurements of muon transmission are indicative of the column of rock traversed ( $\text{g/cm}^2$ ).

The range of muons through rock increases with kinetic energy (Fig. 14). For muography, a key parameter is the muon transmission factor, which is the ratio of muons produced to those that penetrate a distance  $l$ . The continuous slowing down approximation (CSDA) provides reasonable estimates of muon range. With this approximation, the transmission is given by weighted integral of the muon flux:

$$T(l) = \frac{1}{\Phi} \int_{E_m}^{\infty} dE \varphi(E) H[R(E) - l] \quad \text{Eq. 3}$$



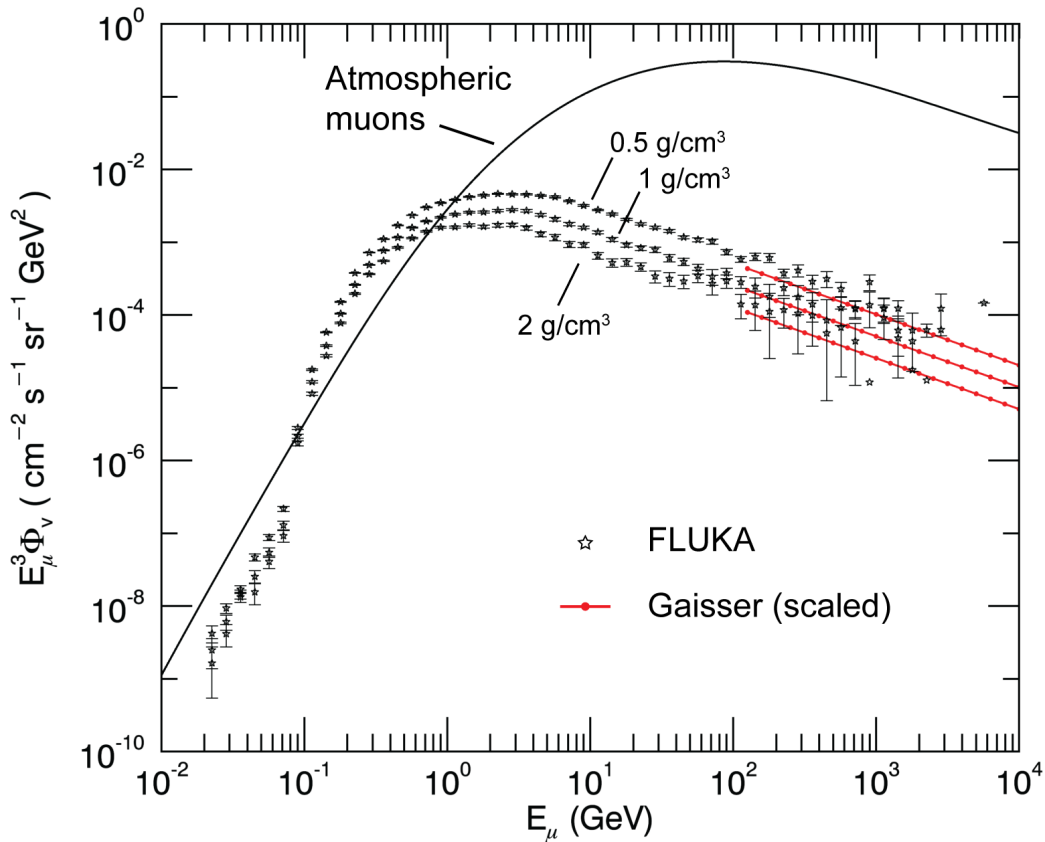


**Figure 12.** Detailed Monte Carlo calculations (via FLUKA) of the vertical muon flux produced in the surface of a rocky airless body are compared to the scaled Gaisser cascade model (Eq. 2). The vertical flux of muons at sea level produced in Earth’s atmosphere is shown for comparison (Allkofer et al., 1971).

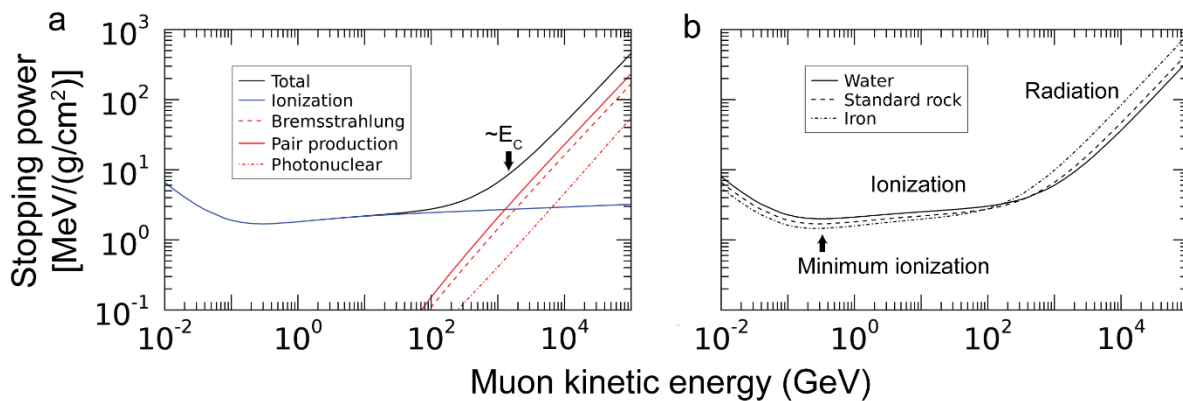


**Figure 13.** Stopping power of muons. a) Stopping power for standard rock (see text) with radiation and ionization components indicated. The critical energy  $E_C$  is where ionization and radiation losses are equal. b) Comparison of stopping power for different materials found on planetary surfaces.

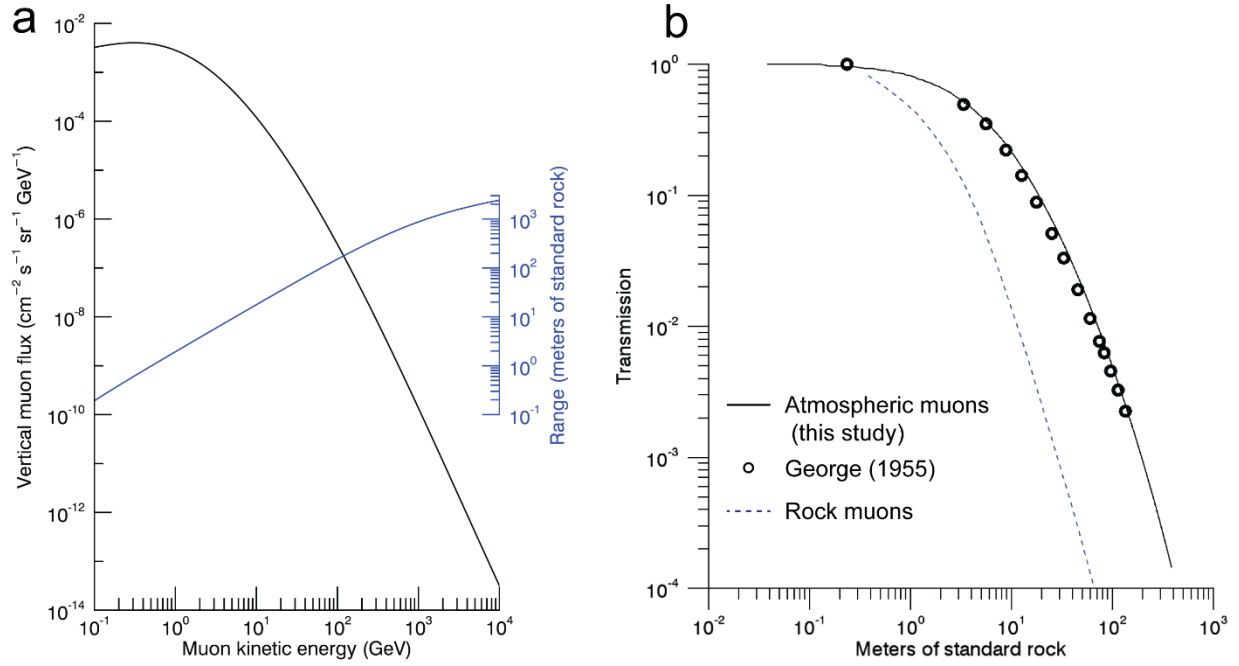


**Figure 14.** Range and transmission of muons. a) The sea-level flux of vertical, atmospheric muons is compared to the range of muons in standard rock ( $2.6 \text{ g/cm}^3$ ). Muons with kinetic energies greater than 10 GeV can penetrate more than 10 m of rock. b) The transmission of atmospheric muons (calculated using Eq. 3) through rock is compared to that determined by E. P. George in 1955 used in the determination of rock overburden within a tunnel. The transmission of vertical muons produced in the outermost ~meters of a rocky asteroid is also shown. The “rock muon” transmission curve is for a FLUKA-calculated asteroid spectrum shown in Fig. 12 ( $1 \text{ g/cm}^3$ ,  $E_m = 1 \text{ GeV}$ ).

The flux of galactic cosmic rays entering the surface of an asteroid varies linearly with the cosine of the crossing angle. If we assume that muons are produced in the same direction as the incident cosmic ray, then muon production can be modeled as a surface current source, i.e.

$$J\left(\left|\hat{n} \cdot \hat{\Omega}\right|\right) = \Phi \left|\hat{n} \cdot \hat{\Omega}\right| \quad (\text{muons/cm}^2/\text{s}/\text{sr}) \quad \text{Eq. 5}$$

where  $\Phi$  is the vertical muon flux (e.g. Eq. 2),  $\hat{n}$  is the unit outward surface normal at the point of crossing,  $\hat{\Omega}$  is the unit direction vector of the GCR, and  $\left|\hat{n} \cdot \hat{\Omega}\right|$  is the magnitude of the cosine of the crossing angle. Assignment of the production of muons to the surface (ignoring their production with depth; cf. Fig. 24), results in a simple model that can be used to explore systematic variations in the through-going muon flux. In this case, the total number of muons emitted from a surface parcel is  $\pi \Phi$  (muons/cm<sup>2</sup>/s).

This results in the following expression for the flux of muons arriving at a point outside the asteroid (cf. Prettyman, Yamashita, et al., 2015):

$$\phi = \Phi \Omega \langle T \rangle \quad (\text{muons/cm}^2/\text{s}) \quad \text{Eq. 6}$$

where  $\Omega$  is the solid angle (steradians, sr.) of the surface parcel viewed from the detector and  $\langle T \rangle$  is the mean transmission factor through the intervening material (Eq. 3).

The flux of muons arriving at a detector is not explicitly dependent on the shape of the source region and depends on the viewing geometry and mean transmission. The former is determined by asteroid shape, but can be partially controlled by experimental design. The latter depends on density of the bulk regolith within the field-of-view. Placement of the detector close to the target is desirable to maximize the solid angle. As will be discussed later, restricting the field of view to the center of the body maximizes the sensitivity to transmitted muons relative to other particle backgrounds.

Equation 6 can be used to estimate through-going event rates for different measurement scenarios. For our Phase II mid-term review, we considered a spherical asteroid with a hodoscope placed on the surface. The hodoscope had a  $1 \text{ m}^2$  area and a half-width opening angle of 37 degrees in order to view the center of the asteroid (Fig. 15a). The event rate was determined by a detailed Monte Carlo transport simulation using the FLUKA code (described in the next section). This calculation showed that the population of muons below 1 GeV is dominated by particles that originate on the same side of the asteroid as the detector. This “spatter” component contributes to the albedo of secondary particles produced by GCRs in the outermost surface. In order to observe the transmitted muons, a practical muon imaging system must reject the albedo component with high efficiency.

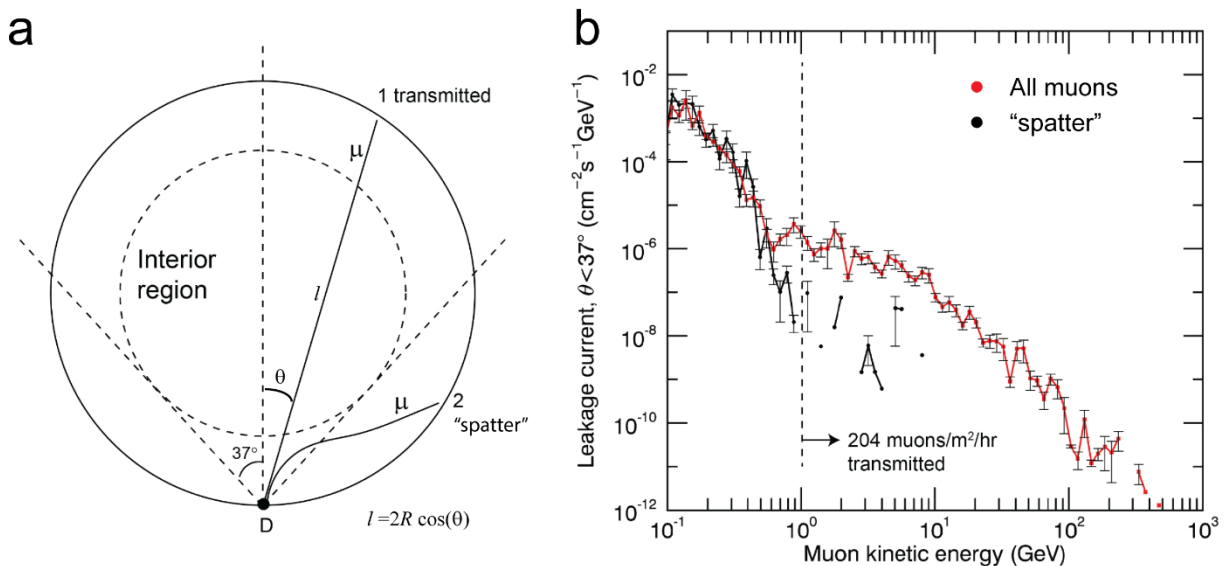


**Figure 15.** Benchmark problem. a) A spherical asteroid of 50 m radius ( $R$ ) and  $0.5 \text{ g/cm}^3$  density is exposed to an isotropic flux of GCRs. The objective is to determine the event rate for through-going muons that travel in approximately straight-line trajectories (1) through the asteroid. The detector (D) is placed on the surface and has a half-angle opening of 37 degrees. Note that chord-lengths through the asteroid  $l$  scale with the cosine of the angle of incidence  $\theta$ . b) A detailed Monte Carlo radiation transport calculation (FLUKA) indicates the current below 1 GeV is dominated by muons that originate on the same side of the asteroid as the detector (labeled 2 in panel a).

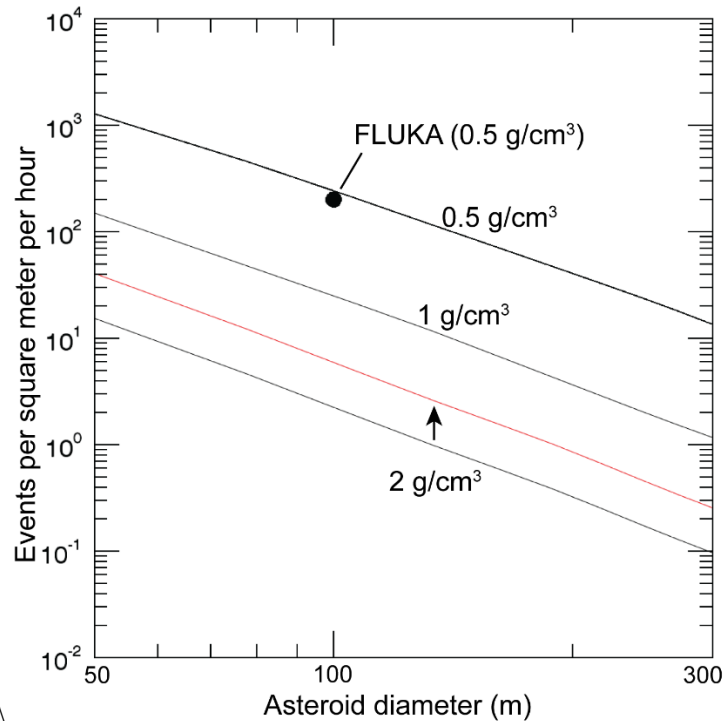


**Figure 16.** The event rate of through-going muons calculated via Eq. 6 is shown for selected densities as a function of asteroid diameter. The red curve indicates the event rate for an asteroid with 0.5 g/cm<sup>3</sup> and 2 g/cm<sup>3</sup> densities for the regolith and bulk, respectively. The FLUKA-calculated rate is shown for a 50 m diameter asteroid with a density of 0.5 g/cm<sup>3</sup> (Fig. 15).

The simple model (Fig. 6) produces similar results to FLUKA for the benchmark problem and can, therefore, be used to explore the systematic variations in event rate as a function of asteroid size and density (Fig. 16). If background contamination is negligible, then the event rates can also be used to determine the sensitivity the technique to interior density contrasts. The red line in Fig. 16 gives the event rates for an asteroid with a low density regolith (0.5 g/cm<sup>3</sup>) and denser interior (2 g/cm<sup>3</sup>). The presence of a low density outer layer would result in over a factor-of-two increase in the event rate compared to a homogenous asteroid. This supports the idea that variations in near-surface density (the presence of fine-grained and rocky regolith regions) could complicate the interpretation of interior structure. Other observations, including characterization of surface morphology using camera data or mapping of relative density using radar, would be needed to disentangle muon production and attenuation.

A more realistic scenario is illustrated in Figs. 17-19 (and the cover page of the report). We developed a small body shape model using the results of simulations of rubble-pile formation by Michel and Richardson (2013) (priv. comm. P. Michel). We used cluster analysis to separate re-accreted aggregates into groups of similar points. Convex hulls of these point sets produce “rocks,” which were combined to form the small body. This process duplicates the “sea otter” shape of the aggregate model, which is similar to that of Itakowa. It also makes voids and fractures that might be found on asteroids and comets.

The data were scaled to produce an object, roughly 200 m in length, shown in Fig. 17a. The solid regions were modeled with a density of 0.5 g/cm<sup>2</sup>, with microporosity consistent with low-

density cometary materials. An image of the chord lengths through the object reveals a heterogeneous interior with a large central void (Fig. 17b).

One possible mission scenario would be to land a muon hodoscope with  $1 \text{ m}^2$  sensing area on the surface of a comet. The goal would be to view the interior density structure from a fixed location and observe how that structure evolves over time (e.g. as the comet passes through perihelion). Fig. 17a shows a target landing site located near the large interior void (Fig. 17b). Assuming a half-angle field of view of 45 degrees, the hodoscope would see a distribution of chord lengths, with a mean of about 100 m (Fig. 18a). The macroporosity along the chords (void space) spans a wide range of values, up to about 0.45 (Fig. 18b), i.e. up to 45% of the comet's interior consists of macroscopic voids.

Using Eq. 6 images formed by the hodoscope were simulated for different integration times (1 day and 10 days, shown in Figs. 19a and b, respectively). The cover page shows an image accumulated over 30 days. In each case, the sampled events were resampled to form a  $50 \times 50$  image. The event rate was about 420 per hour. So, the image accumulated during a single day includes about 10,000 events and the 10-day image includes 100,000 events. A day of integration is more than adequate to sense the interior void (Fig. 19a). Ten days of accumulation begins to resolve small structural details, such as the "rock" indicated by the arrows in Figs. 19b and c.

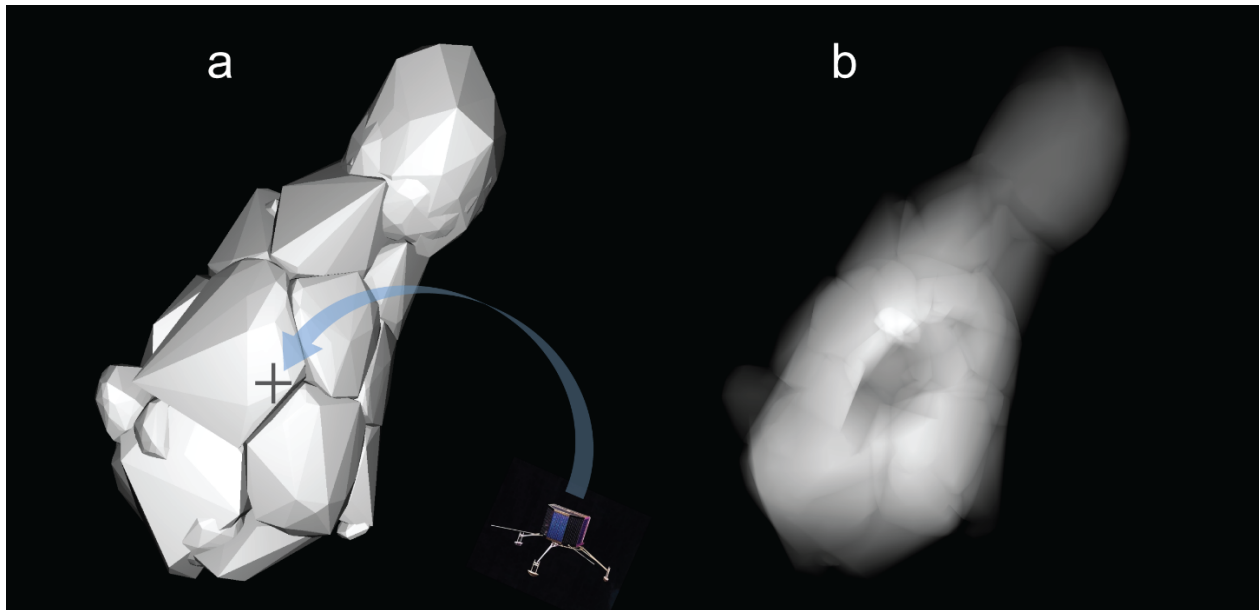


**Figure 17.** A simulated comet, roughly 200 m in length, contains solid regions with low microporosity along with macroscopic cracks and voids. A possible mission scenario would be to land a large-area hodoscope on the surface to observe the interior structure and watch how it changes as the comet passes through perihelion. a) The “+” marks a landing possible landing site. b) A chord-length image reveals intricate interior structure, including a large void beneath the landing site.

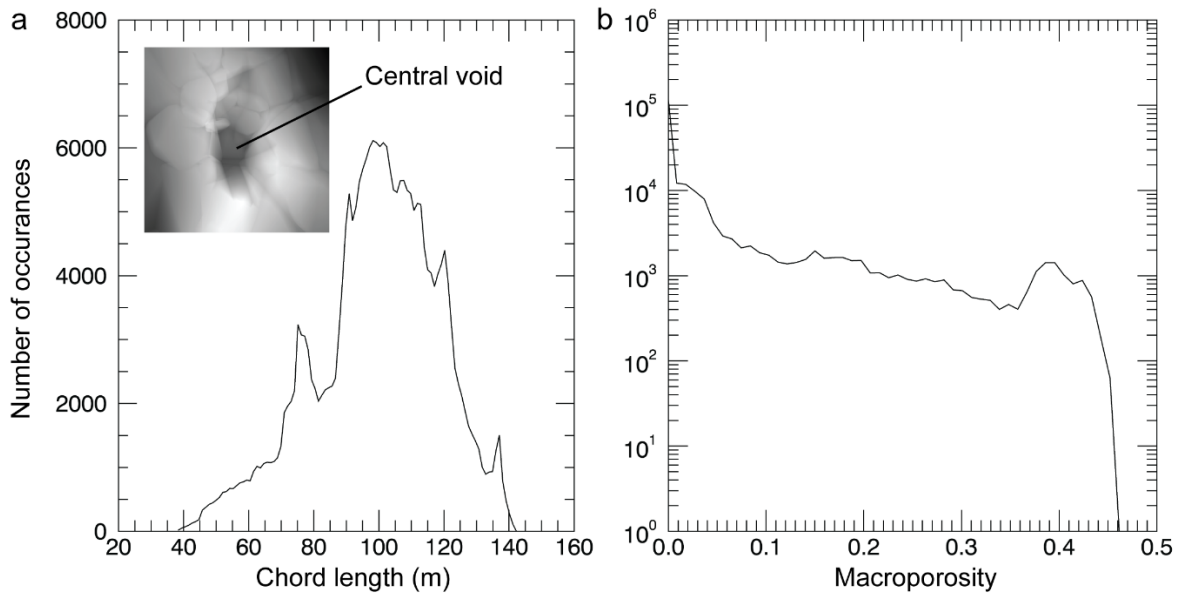


**Figure 18.** a) The histogram of chord lengths sampled by the hodoscope is shown along with a chord-length image (inset). b) The corresponding histogram of macroporosity is shown. For each sampled direction, macroporosity was determined by dividing the length traversed through void by the total distance through the comet. The large central void takes up about 40% of the asteroid in the vicinity of the lander.

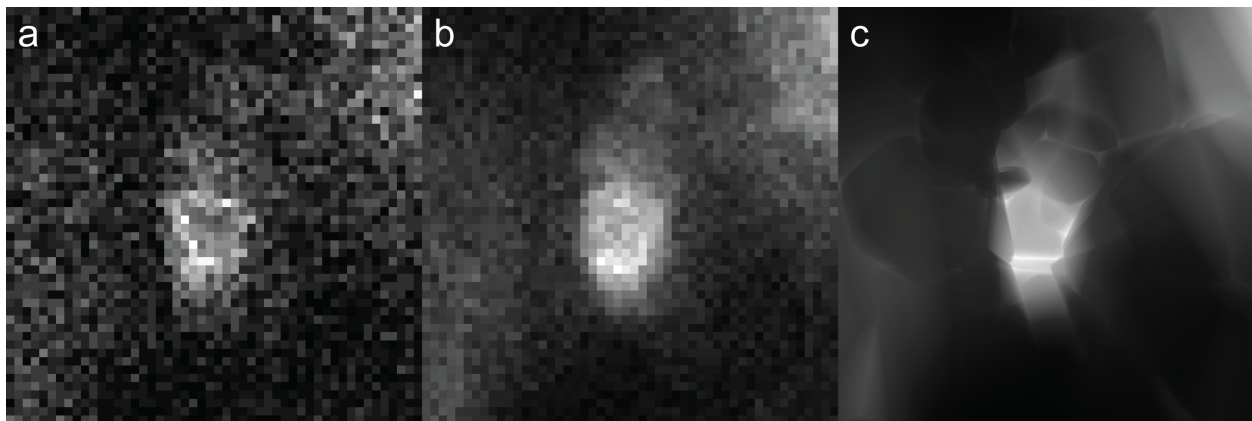


**Figure 19.** Simulated hodoscope event data for a) 1 day of accumulation (roughly 10,000 events) and b) 10 days of accumulation (about 100,000 events). Sampled directions were binned onto  $50 \times 50$  pixels. c) An ideal, high-resolution event image, showing the finely-detailed interior structure of the simulated comet.

Simulations of event data from the example comet mission show that muography is potentially a powerful tool that could be used to determine the interior structure of small bodies. Muography could work, as long as the high-energy, through-going muons can be separated from various high-intensity backgrounds. These include direct interactions of cosmic rays with the hodoscope (a downward flux in the case of a landed mission) and the interaction of the secondary particle “spatter” originating on the same side of the object as the sensor. In addition, some means is required to map the density of near-surface regions where the muons are produced. In the next section, we discuss radar as a possible method for mapping regolith density. In subsequent sections we use detailed end-to-end simulations of muon production, transport, and detection to identify a feasible design for a muon imaging system for the target applications.

## Radar constraints on regolith density

There are several parameters that can be chosen for a radar system for use on small bodies. One is the observing frequency/wavelength. Typical surface penetration depths are of order 10 wavelengths, so lower frequency (longer wavelength) radars penetrate the surface farther. However, the spatial resolution of a radar is obtained by modulating the radar wave, and as it is not possible to modulate a low-frequency radar at a high frequency, low frequency radars will tend to have relatively low resolutions, both into the surface (by modulation) and on the ground (due to diffraction).

For this reason, a bulk-sensing method like muography would be best combined with higher-frequency radar, which would allow high-resolution sensing of the upper few meters of surface regolith (using a  $\sim 10$ -cm radar wavelength).

Radar interaction with surfaces consists of refraction in dielectric media and reflection from dielectric contrasts. Dielectric contrasts show — for example — the layers in the Martian Polar Layered Terrain as a series of layers in a SHARAD scattergram. Interpretation of the actual material densities using radar is however quite difficult and ambiguous. In the case of the Martian Polar Layered Deposits, where we have visible-light images of the layers (to measure thickness), an expectation of relatively uniform layering over the scale of the radar beam (locally plane-parallel), and an a priori understanding of the bulk dielectric material (water and CO<sub>2</sub> Ice), it is possible to model the electromagnetic scattering and infer details about the other material properties (e.g. Nunes & Phillips, 2006). However, for scattering from an irregular surface of unknown detailed composition, it is relatively straightforward to observe density contrasts, as they appear as layers, but the absolute dielectric properties would be extremely difficult to uniquely determine.

Proposed small-body radar instruments operate in one of two modes: Transmission radars require separate stations for transmission and reception. Transmission radar in principle allows a measure of the bulk dielectric constant by measuring loss and time delay, though it is technically challenging due to the multiple stations and coordination of precise timing of signals between stations, and the small reflections from layers are difficult to measure. Reflection radars measure only the reflections from boundaries, and so are good for probing structure. Long-wavelength reflecting radars that penetrate the surface will suffer from ambiguities between the subsurface structure and the surface topography, though this ambiguity may be resolved with a sufficient number of observations (e.g. Sava & Asphaug, 2018).

An example relevant to this study is 101955 Bennu, a small, carbonaceous asteroid that was imaged by ground based radar prior to its exploration by OSIRIS-Rex. Radar data were acquired using the Arecibo Observatory's 12.6 cm radar and the Goldstone tracking station's 3.5 cm radar. The data provide constraints on near-surface, bulk density ( $0.9 \text{ g/cm}^3$  "Eros calibrated"). The bulk density of Bennu determined by OSIRIS-Rex is similar ( $1.19 \pm 0.13 \text{ g/cm}^3$ ); however, Bennu's surface is much rougher and more heterogeneous than implied by radar polarization ratios, which indicated a relatively smooth surface on cm-scales. The implications for the acquisition of orbital radar data given OSIRIS-Rex observations would be a useful future study.

## Use of FLUKA for GCR simulations

FLUKA is a fully integrated particle-physics, Monte Carlo simulation package (Böhlen et al., 2014; Ferrari et al., 2005). FLUKA was originally introduced to aid in the shielding design for the CERN Proton Synchrotron (PS) in the early 1960s. More recently it is used for a wide range of applications including high energy particle physics, medical physics, radio-biology, and of relevance here, to simulate cosmic ray and cosmogenic muon-induced backgrounds in deep underground experiments. The design and development of FLUKA is based on the implementation of verified fundamental physics-based models of the various physical processes. FLUKA uses these models in a way that maintains consistency among all reaction steps and types. Thus, all conservation laws are enforced at each step and the predictions have been benchmarked against experimental data, if possible, at the level of single interactions. As a consequence of this consistent approach, predictions for complex simulation problems are robust and arise naturally from underlying physical models. Depending on the validity of the employed models, FLUKA is expected to provide reasonable results even in cases where no direct experimental data are available. Details about FLUKA and a description of the implemented physics models can be found in a recent overview (Battistoni et al., 2015) as well as in the FLUKA manual (Ferrari et al., 2005) and additional material available through the official FLUKA website at <http://www.fluka.org>. The version of FLUKA used for the present study is FLUKA2011.2, from November 2011.

In recent years, there has been an increasing interest in the assessment and modeling of Galactic Cosmic Rays (GCR) particularly in regards to radiation effects on aircraft crew and passengers, astronauts in Low Earth Orbits (LEO) and in interplanetary missions as well as on-board micro-electronics in the space radiation environment (Koontz et al., 2010; Roesler et al., 2002; Trovati et al., 2006). However, the successful application of FLUKA to GCR related issues has a long tradition. For example, a careful comparison between FLUKA predictions and measurements of the muon flux at various altitudes in the atmosphere accurately predicted the results from the balloon-born CAPRICE experiment (Battistoni et al., 2002). Further, the production of muons through GCR interactions with the atmosphere and their transport to earth's surface and down into the Laboratori Nazionali del Gran Sasso (LNGS) were validated with respect to measurement by the MACRO experiment (Ahlen et al., 1993; Ambrosio et al., 1995) as well as the BOREXINO experiment. The muon angular distributions as found for Hall B at LNGS are given in Fig. 20. The muon azimuthal (left) and zenith (right) angular distributions at LNGS for the polar coordinate system pointing up and North with clockwise increasing angle are shown. The blue lines present the results from the more recent data taken by the BOREXINO experiment (Bellini et al., 2013) located in Hall C, and the green lines present the MACRO data (Empl et al., 2014). The black lines represent the FLUKA predictions for BOREXINO, and red line represents the FLUKA predictions with the zenith angle limited for MACRO. Excellent agreement is found between experimental data and predictions, in particular, given that the simulation started with the GCR impinging on the Earth's atmosphere at 70 km altitude.

Single Event Effects (SEE) are not limited to high altitude or in the space radiation environment because of ever smaller integrated circuit feature sizes and the corresponding lower operating voltages. These effects can arise from low energy muon interactions. Historically, reliable data were only available above 200 MeV muon kinetic energies, however, a recent FLUKA study (Infantino et al., 2016) has succeeded in comparing the predicted muon flux down to stopping

muon kinetic energies with the experimental data that are now available (Blackmore et al., 2015) and reports very good agreement.

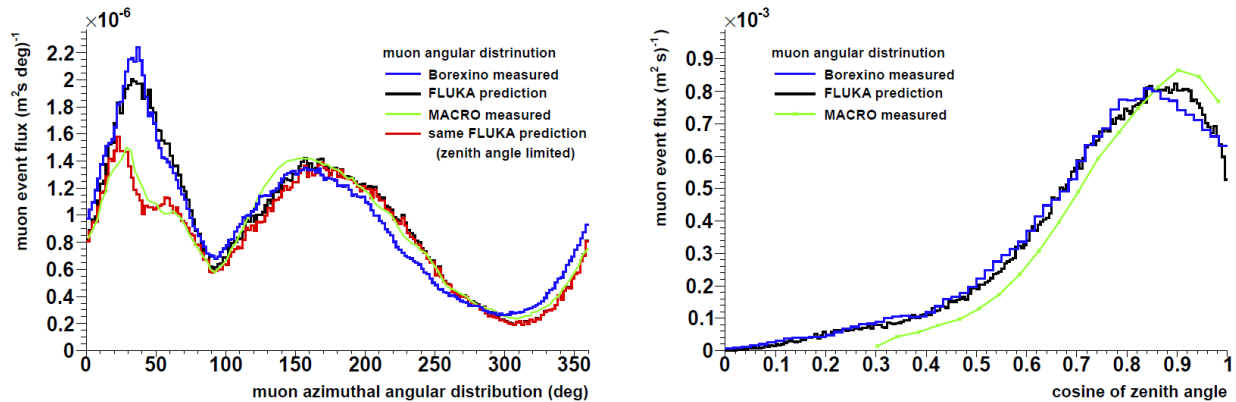


**Figure 20.** The muon azimuthal (left) and zenith (right) angular distributions at LNGS for the polar coordinate system pointing up and North with clockwise increasing angle. Blue line: BOREXINO data, green line: MACRO data, black line: FLUKA predictions, and red line FLUKA predictions with the zenith angle limited for MACRO. Caption and figure from Empl et al. (2014).

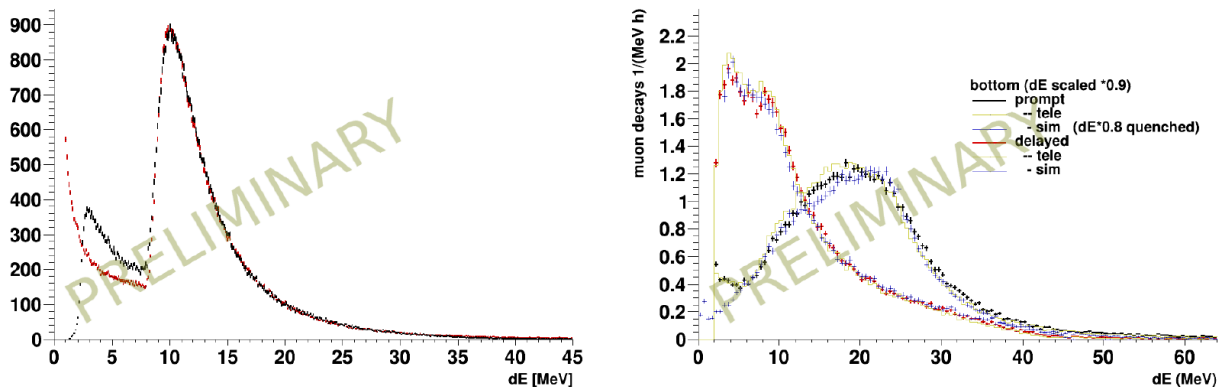


**Figure 21. Left:** The energy-deposition spectrum in a 5 cm thick plastic scintillator from energetic muons as measured by MINIDEX is shown in black with the spectrum predicted by FLUKA in red. **Right:** The energy-deposition spectrum from stopping muons in black with the predicted spectrum from FLUKA in blue symbols. Also shown are the respective decay spectrum of electrons/positrons as measured in red, with the FLUKA predictions again shown in blue.

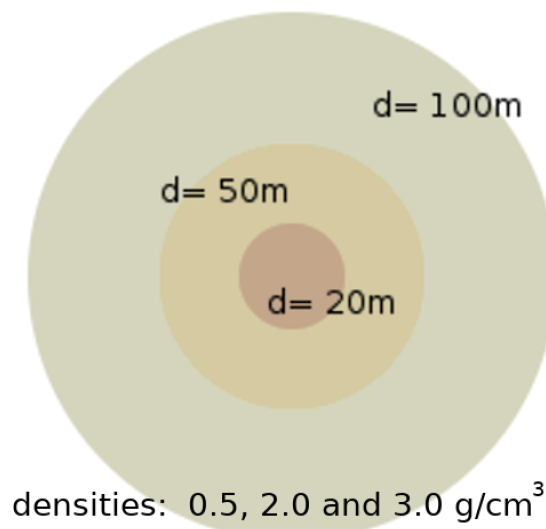
A current experiment, MINIDEX (Abt et al., 2017; Du et al., 2018), that is designed to study muon-induced neutrons produced in lead at a shallow depth, is located in the Underground Laboratory at the University of Tübingen. It consists of several large plastic scintillators used to select crossing muons and two high-purity germanium detectors to identify neutrons via capture on hydrogen. Again, FLUKA is used to predict the muon radiation field at the experimental site, starting with GCR production high in the atmosphere. The energy deposition spectra from the scintillation counters are shown in Fig. 21 to demonstrate the quality of agreement achieved. The spectra on the left are measured and predicted for energetic muons crossing the lead target while the graph on the right is found for muons stopping within the scintillator and the respective

charged muon decay secondaries. This low energy part of the muon spectrum is rather sensitive to a set of parameters (for example, the Earth's magnetic field, the phase of the current solar cycle, the local season of the year at the detector and the details of the composition of the overburden). Still, at this point, the absolute agreement with simulation is found to be within 20% (A. Empl, Fluka based simulation in support of the minidex experiment, Technical Note, MPI, München, March, 2016).

## Asteroid simulations

The potential asteroid objects are simulated as homogeneous spheres. Their composition is modeled after typical regolith, with a variety of densities ranging from 0.5 g/cm<sup>3</sup> up to 3 g/cm<sup>3</sup>. As shown previously (Prettyman et al., 2014), the potential for the investigation of the interior of asteroids through the measurement of penetrating of cosmogenic muons (muography) is only expected to be feasible in a timely fashion for smaller objects. For this study, asteroids of 20 m, 50 m and 100 m diameter were investigated. In a first step of the simulation these spherical objects are subjected to an isotropic flux of GCR protons with kinetic energies from 10 MeV up to 50 TeV, following the most recent predictions from the Badwar O'Neill model (O'Neill et al., 2015).

Spherical dimensions and solid densities used in the FLUKA asteroid simulations.



The simulation was biased in order to favor high energy events to allow the efficient production of those statistically rarer events. Protons constitute approximately 90% of the primary GCR spectrum. In principle FLUKA is available to simulate the all particle GCR spectrum, however, for this initial study the GCR were limited to protons.

All secondary particles exiting from the asteroid are recorded when they cross a shell placed 1 meter above the surface. That height was selected to provide sufficient space for structural components to secure the detector on the asteroid while keeping that distance relatively short in order to minimize the background from decay muons originating from nearside albedo meson decays that were described in Phase-1 of this study (Prettyman et al., 2014). The outputs from this simulation are saved for use as input in subsequent FLUKA simulations to address the proposed detector design.

## GCR induced secondary particles emerging from the asteroid

A spherical asteroid of 100 meter diameter and average density of 2 g/cm<sup>3</sup> is used as an example case here. As shown in Fig. 22 on the left, the flux of secondary particles (multiplied by their kinetic energy) leaving the asteroid is given at 1 meter above the surface. Neutron (yellow symbols) and gamma (cyan symbols) spectra are shown, however, these neutral secondaries are not further considered in this study. Albedo secondary protons (black), pions (green) and electrons/positrons (red) dominate the spectrum over produced muons (blue), even at large kinetic energies. The situation improves when considering the direction of the secondary particles. For muons to convey information about the asteroid interior they will need to pass close to the center, hence their exit direction will need to be close to the surface normal. Restricting secondary particle trajectories to point along the surface normal within 30 degrees will modify the secondary particle spectra as indicated by the graph on the right in Fig. 22.

While the integral total number of muons are still generally outnumbered with respect to the other particle types, as can also be seen in Fig. 22 right, if one considers only energetic secondaries with kinetic energies in excess of approximately 1 GeV, one can achieve access to a rather clean muon signal. Thus, we shall focus on a detector design that can isolate and identify these muons.

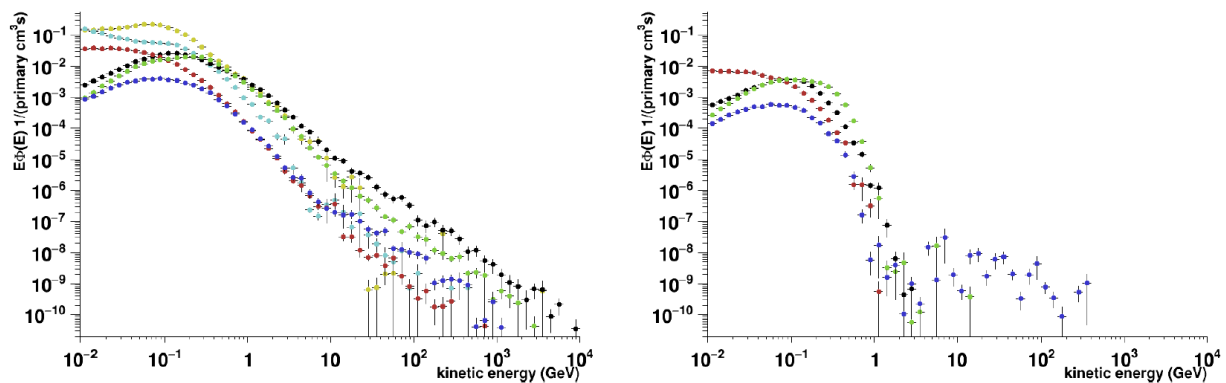


**Figure 22.** **Left:** The kinetic energy spectra for secondary particles leaving the asteroid are shown with neutrons in yellow, gammas in cyan, protons in black, mesons in green, electrons/positrons in red and muons in blue. **Right:** The same information is plotted for charged secondaries restricted to only those whose direction falls within 30 degree of the asteroid surface normal. Note the separation of the muons for kinetic energies above 1 GeV.

### Albedo muon and energetic electron/positron backgrounds

A careful examination of the origin of the muons exiting the asteroid's surface reveals that two distinct GCR induced muon populations exist. This is apparent from the blue spectrum shown on the right plot in Fig. 22 where there are an abundance of muons with the same spectral shape as the other charged particles with kinetic energies below 1 GeV, and a second distinct spectrum above 1 GeV. These two populations can be emphasized by graphing the distance distribution between GCR entry point and the secondary muon exit point at the asteroid surface as function of the muon track opening angle with the surface normal. This is shown, indicating several muon kinetic energy bands by different color symbols, on the left in Fig. 23. A clear correlation between path length and direction identifies predominantly energetic (red symbols) through going muons as opposed to low energy albedo type muons (blue symbols). This separation is

very clean for muon directions within 30 degrees of the surface normal, i.e.  $\cos(\theta) > 0.866$ . The low energy albedo muons, which form an ultimate background as they are the signal particle type, can be suppressed by selecting muons with kinetic energies above approximately 600 MeV.

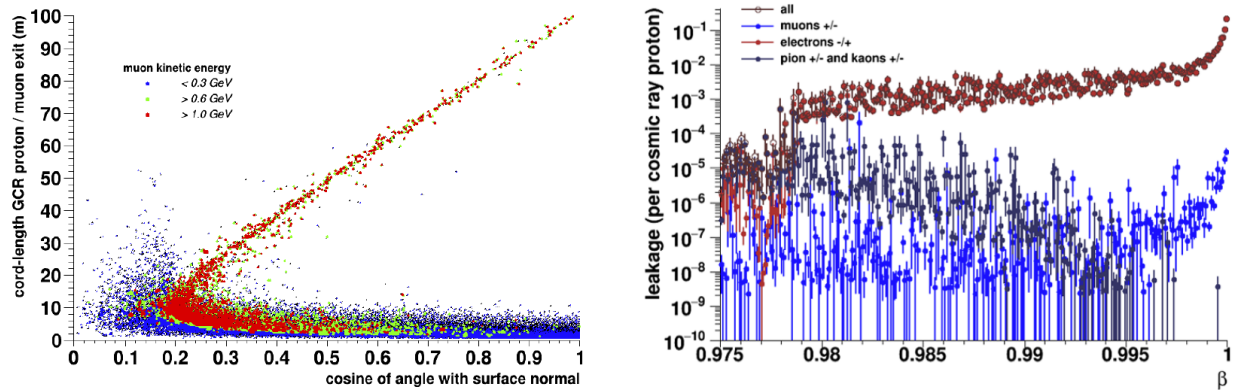


**Figure 23. Left:** The distance between the GCR entry point and the muon exit point (cord-length) is shown as a function of the cosine of the muon track angle with the asteroid surface normal. Muons selected for  $E_{kin} < 0.3$  GeV are given by in blue symbols, for  $E_{kin} > 0.3$  GeV and  $< 1.0$  GeV by the green, and  $> 1.0$  GeV in red symbols respectively. **Right:** The velocity spectra as a fraction of the speed of light for particles exiting the asteroid surface are plotted with focus on the electron/positron (red symbols) as compared with the mesons (black symbols) and the muons (blue symbols). For muons above 600 MeV (velocity  $> 0.987c$ ), the only background as a function of kinetic energy are the electrons.

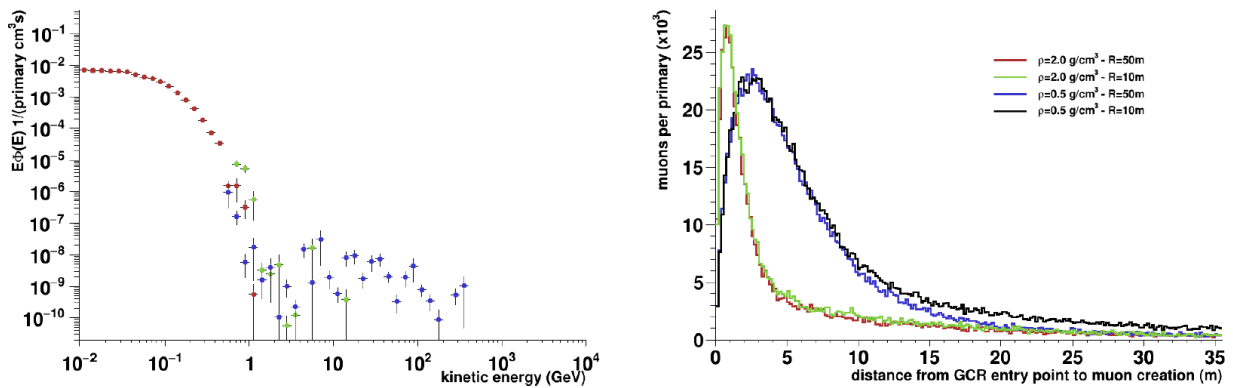


**Figure 24. Left:** Kinetic energy spectra for secondary particles (electrons/positrons in red, pions in green and muons in blue) leaving the asteroid with a direction within 30 degrees with respect to the surface normal and with a velocity  $\beta > 0.987$ . **Right:** Muon production location as a function of distance to GCR entry point at the asteroid. Given for 20 m and 100 m diameter asteroids with density of  $2.0$  g/cm<sup>3</sup> (green and red lines respectively) and  $0.5$  g/cm<sup>3</sup> (blue and black lines respectively).

As a practical matter, we shall assume that only the velocity  $\beta$  of particles, as opposed to their kinetic energy and specific particle type identification is directly measurable along with the particle direction with respect to the local vertical for a detector envisioned for a mission to an asteroid or comet using current technology. Thus, the predicted velocity spectra for muons (blue), mesons (black) and electrons/positrons (red) are shown on the right in Fig. 23. The velocity for a muon with a kinetic energy  $E_{kin} = 600$  MeV is  $\beta = 0.987$ . Assuming a Cerenkov

detector with a threshold near  $\beta = 0.987$  to discriminate against low energy particles one finds the remaining particle fluxes as shown on the left in Fig. 24. Given that the electrons and positrons are highly relativistic even at low energies, they present the primary remaining background to be eliminated.

### Small asteroids with low density

The reduced muon production by mesons inside the asteroid material as opposed to the production in the thin, high altitude atmosphere surrounding earth, was detailed during the Phase I study. The distance between the GCR entry point at the asteroid and the location of the muon production is shown on the right in Fig. 24 for a 100 meter diameter asteroid of  $2.0 \text{ g/cm}^3$  (blue) and  $0.5 \text{ g/cm}^3$  (black) average density. In case of low density, a large fraction of the cosmogenic muons will be produced close to the center rather than near the surface for small asteroids. For an assumed density of  $0.5 \text{ g/cm}^3$  and a 20-meter diameter asteroid some fraction of muons are even produced past the asteroid center. This will complicate the interpretation of the through-going muon signal even though an increased rate of these muons is predicted as they require less kinetic energy to penetrate the object.

### Detector simulations

In general, the detector is envisioned to cover a disc of approximately 1 m diameter. It is expected to consist of several layers in order to measure charged particle tracks. A number of virtual cylindrical volumes with 50 cm radius and 35 cm height were placed in a second step of the simulation. These were located 115 cm above the asteroid and cover the entire surface. In Fig. 25 the fully covered 100-m diameter asteroid is pictured as an example, with a close-up on the right. Secondaries entering any one of the virtual discs, even through the side walls, were recorded and their coordinates transformed to coincide with a single virtual cylinder at the nominal 'top' position. For the illustrated case of the 100 m diameter asteroid somewhat more than 75% of the surface was effectively considered in this way for the actual detector studies.



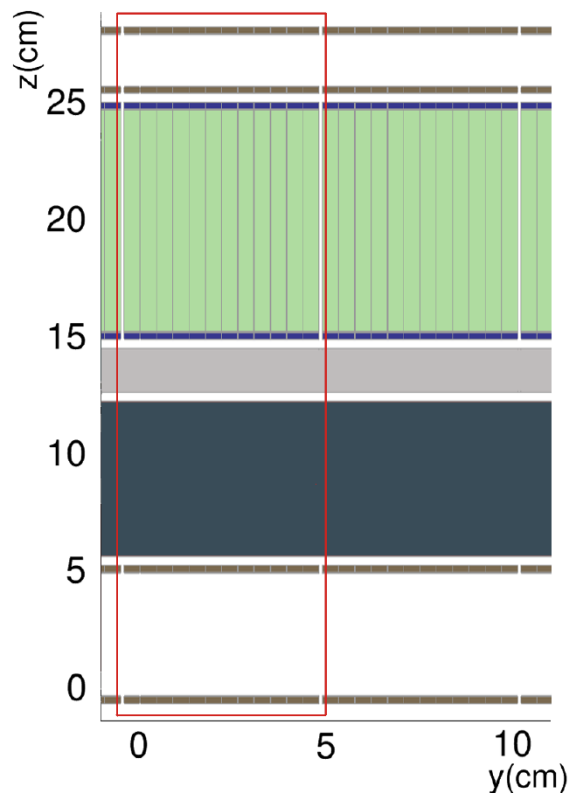
**Figure 25.** Fully covered 100 m diameter spherical asteroid. An enlarged view of a small section is given on the right. The small cylinders are just a little larger than the implemented detector setup. For technical reasons the sphere had to be covered in 8 identical sections.

In the third step of the simulation, the actual detector design was implemented within the virtual cylindrical volume and exposed to the previously recorded secondary incident particle radiation field. Note that there is an absolute requirement for the detector to discriminate against the ever-present downward moving incident charged particles whose tracks lie with 30 degrees of the local detector vertical.

### Preliminary detector design

A zoomed cross-sectional view of the preliminary detector design is shown below. The detector setup is intended to be deployed onto the asteroid at approximately 1 m above the surface with the detector vertical determined with respect to the direction towards the relative center of the asteroid body. The individual detector components and their specific purpose will be outlined below. In order to discern which energetic muons crossed the asteroid interior, the device will need to distinguish the direction of outward moving particles as well as eliminating all background particles to the muon signal above 600 MeV. The proposed initial setup consists of several layers of pixelated silicon semiconductors or comparable scintillation-based elements for tracking (dark brown). Similarly, sensors in the form of Silicon Photo Multipliers (SiPMs, dark blue) are used to read out optical signals on both sides of aerogel based Cerenkov radiator pixelated cells (light green).

Cross-sectional view of the preliminary detector design.



To enhance the signal of minimum ionizing muon tracks, and essentially eliminate the albedo electron backgrounds, passive scattering/absorption layers made of iron (dark blue) and aluminum (light grey) are placed between the tracking sensor planes. The tracking sensors have a

4×4 mm<sup>2</sup> footprint and are arranged in modules of 12×12 units - one such unit being indicated by the red outline in the previous figure. A top view of a module is given in Fig. 26 on the left while their arrangement onto a disc of approximately 1 meter diameter is indicated on the right with a single module shown in red. The total active area is 7900 cm<sup>2</sup>. The overall thickness of the detector setup is approximately 35 cm. A 3D rendering of the entire detector is shown in Fig. 27. A list of required detector capabilities together with the associated relevant detector component is given below.

- Up-down discrimination to reject downward moving primary GCR - The overall height of the detector setup is on the order of 35 cm with several layers of tracking devices. Fast pixellated silicon detectors with a small footprint are proposed for this task. At the speed of light a particle will have a time difference of approximately 1.0 ns between crossing the outer tracking layers. The ability to obtain Time-Of-Flight (TOF) resolutions of better than 200 ps has been deployed in existing and planned accelerator experiments (Böhm et al., 2016) which will provide a clear time order for hits in the tracking layers to unambiguously determine the up-down direction of the track, as well as being of considerable assistance in associating hits in the different tracking layers as being associated with the same physical event time order for hits in the outermost detector planes.
- Track information is used to require the trajectory to point back into asteroid (within 30 or 40 degree with respect to the surface normal) and to determine the quality of the 3D straight line fitting. Four tracking layers are provided in addition to the 2 optical sensor planes which are expected to simultaneously function as tracking sensors (see below).
- Suppression of the large albedo type background, in particular from electrons, is required in order to identify muons. A substantial amount of material to absorb low energy electrons and cause charged particle scattering is placed between the tracking devices below the Cerenkov detector cells. Muons, which straggle significantly less than other charged particles, can be singled out by the quality of straight tracks throughout the entire setup. With a 7 cm thick layer of iron and a 2 cm thick layer of aluminum the total mass of the absorber material is 478 kg.
- Given the fine segmentation of the active detectors and their time resolution, the proposed system has a high rate tolerance and will permit the identification of single track events with high efficiency. Even with a GCR flux of approximately 1 per (s cm<sup>2</sup>), individual sensors are expected to trigger at a rate of < 0.2 Hz.
- Making use of aerogel Cerenkov cells will permit the implementation of a muon kinetic energy threshold of approximately 0.6 GeV. This will address the critical albedo muon background and some of the albedo meson background. As radiator material one could select commercially available aerogel with a refractive index  $R_f = 1.013$  which relates to a muon kinetic energy  $E_{kin} = 0.56$  GeV for the onset of light production. The produced light is to be recorded by fast SiPMs.
- Reading out both sides of the aerogel radiator cells would enable a direct in-situ measurement of the energetic component of the incoming GCR flux. In addition, it also offers a redundant way to discriminate up/downward moving charged particles.

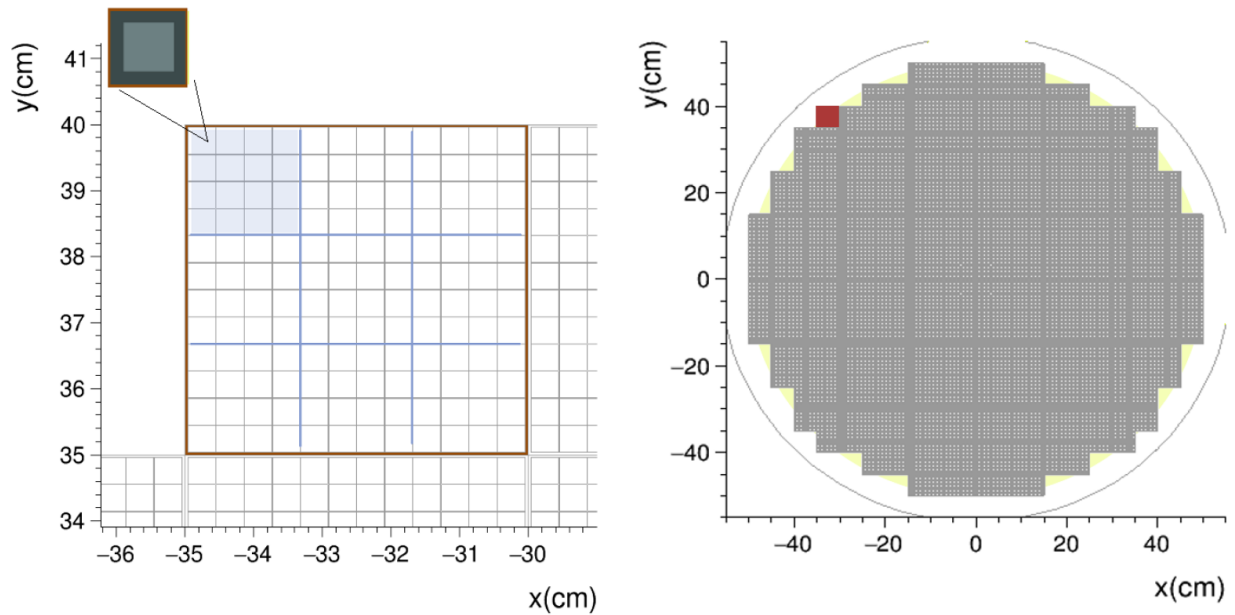


**Figure 26.** Top view of the implemented silicon tracking devices for a single sensor module (**left**) and the full detector configuration (**right**).

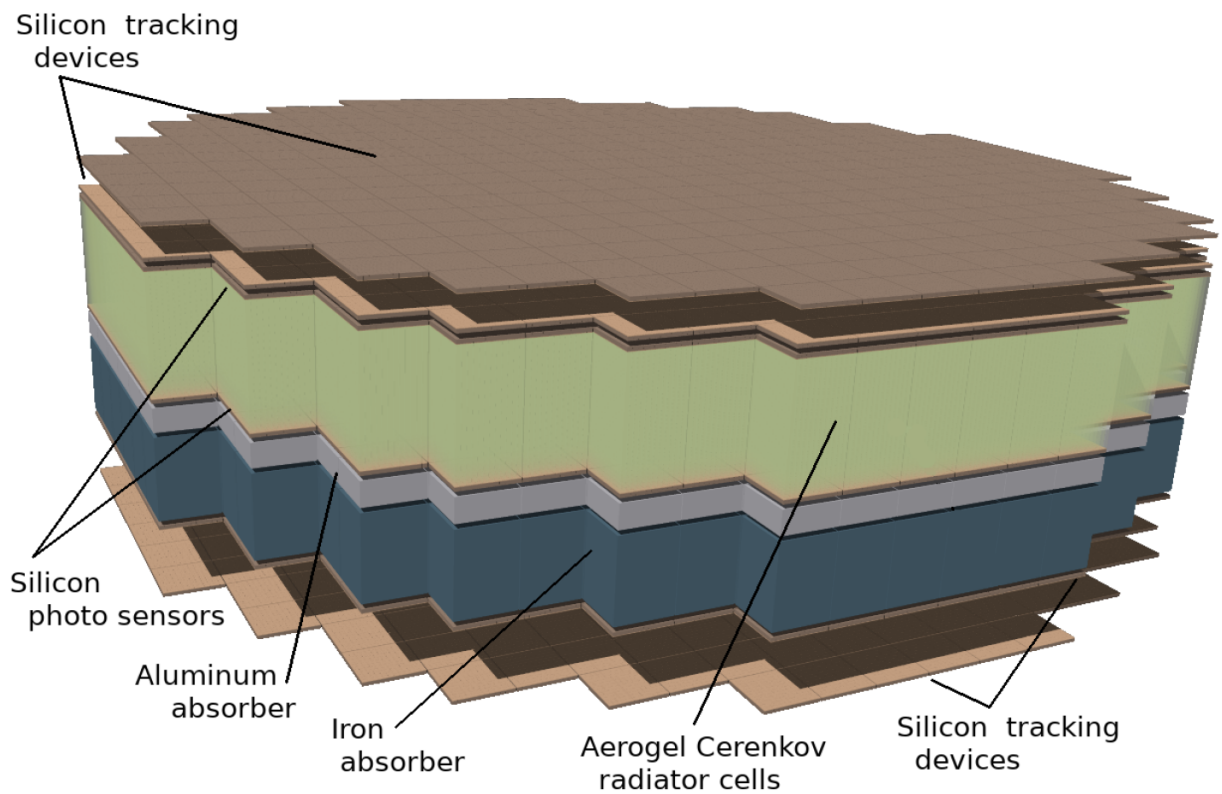


**Figure 27.** View of the FLUKA implemented detector geometry. Toward the asteroid surface Fe and Al absorbers are placed. These are followed by the aerogel cells. Double tracking layers are placed underneath the absorbers and above the Cerenkov detector layer. The Cerenkov detector cells are viewed by fast SiPM based optical sensors.

## Detector performance

At this point, sensor efficiencies and detector resolution or noise are not addressed. For the passive absorber a combination of iron and aluminum was selected after a study regarding the efficiency of absorbing and scattering electrons in particular. A similar response was obtained by using lead as absorber, however, the selected materials are less problematic to incorporate into the detector design and could, at least in part, simultaneously serve a structural purpose.

As an example a 100 m diameter asteroid with a density of  $2.0 \text{ g/cm}^3$  will be considered. The integral average rate of GCR as found from the implemented Badwar O'Neill model predictions is 0.98 primary cosmic ray per  $\text{cm}^2$  per second. Hence, the instrument is expected to be traversed by approximately 7740 direct, downward moving GCRs per second. The predicted rates of upward moving secondary particles are listed in Table 2. These are predominantly albedo type secondaries. Only charged particles are taken into account. Incident energetic gamma rays as well as the locally produced albedos will cause some effective random noise events in the active detector elements, but at a low enough level to have only a minor impact on the net efficiency to identify the muons of interest here. Given both downward and upward moving particles and photons entering the detector, a total signal rate of approximately 10 kHz is expected.

**Table 2.** Integral rate of upward moving charged secondary particles, induced by GCRs in the asteroid, entering the detector per second. The Monte Carlo 1-sigma precision is indicated.

Asteroid diameter	100 m	50 m	20 m
muons	$106.8 \pm 0.6$	$102.0 \pm 1.1$	$105.2 \pm 0.9$
electrons	$1762.0 \pm 4.1$	$1785.6 \pm 6.7$	$2079.6 \pm 6.7$
protons	$625.6 \pm 1.1$	$629.9 \pm 4.3$	$740.3 \pm 8.1$
pions	$489.2 \pm 0.9$	$504.4 \pm 1.7$	$583.0 \pm 3.3$
kaons	$2.3 \pm 0.1$	$2.6 \pm 0.1$	$4.4 \pm 0.2$

For smaller asteroid sizes of 50 m and 20 m diameter, the albedo flux is predicted to increase by about 2% and 17% respectively because of the larger curvature.

### Albedo electron suppression

Besides recording muons which are exiting the asteroid surface, the most important aspect of the detector design is to identify and/or suppress albedo type background events. Of this background, electrons are the most copious and complicated component to address. The employed passive absorber and scattering material removes a substantial fraction of the low energy electrons and mesons. High energy electrons are more likely deflected while energetic mesons have an increased chance to create secondaries through hadronic interactions. Given a detector design as outlined earlier, four different selection criteria are employed to obtain a data sample with a high fraction of through-going cosmogenic muons.

### Direction of particle tracks

In order to learn about the asteroid interior muons are required to pass close to the asteroid center. Particle directions within 30 degrees of normal to the asteroid surface are selected. This requirement also reduces the fraction of albedo type particles as these are less likely emitted normal to the surface.

### Single particle events

Muons will create secondary particles by electromagnetic processes: bremsstrahlung, pair production and ionization (delta electrons) as well as muon-nuclear inelastic scattering. However, the rate of production per path length is low and a large fraction of the through-going muons are expected to emerge in single charged particle events. Depending on the overall rate of particles crossing the detector planes and the tracking detector response time, it may be necessary to consider a localized veto area surrounding potential muon tracks. The selection will again reduce the fraction of albedo type events since the local GCR hadronic interactions are likely to produce multiple charged particles emerging from the surface. As the time resolution technology improves, the losses from incidental coincidences will decrease. For example, although a gaseous-based, large-area MRPC tracking planes at the ALICE experiment at the LHC have achieved  $\sim 60$  ps resolution with fluences as high as 10,000 tracks per square cm.

### Minimum particle velocity

Making use of the aerogel Cerenkov detector cells particle tracks with an approximate velocity  $\beta > 0.987$  are selected. This requirement removes further particles with low energy after passing the absorber together with albedo type muon candidates. SiPMs with the same pixel size as used for the tracking sensors are proposed as optical detectors in order to address the rate of crossing charged particles. However, for practical reasons, the aerogel radiator can use a coarser structure, permitting several photo sensors to read out individual cells. For example the aerogel radiator could be segmented optically to fit units of  $4 \times 4$  sensors with a cell size of  $1.6 \times 1.6 \text{ cm}^2$ , or more conservatively, to fit sensor modules instead with a  $5 \times 5 \text{ cm}^2$  cell size.

### Straight track fitting

Finally, particle track candidates which pass the above selection criteria and caused hits in all tracking planes are subjected to a 3D straight line fitting routine. A set of example fitting results are shown in Fig. 28. The larger scattering for hits from electron type tracks is indicated. Tracks for very high energy electrons (order GeV) will appear like muons, however, electrons at these energies are rare and if directed close to the surface normal, are likely part of the through-going muon signal.

The impact of the detector pixel size on the track fitting quality has not been taken into account. Nominal optical properties were implemented for the aerogel radiator and photons were only counted if they reached the top or bottom face viewed by the SiPM. An overall cathode quantum efficiency of 30% was assigned to the SiPM. The performance of the simulation in regards to the optical photon production, transport and detection was studied and a realistic performance of Cerenkov radiator and SiPM sensors assumed for the analysis (e.g. Asaturyan et al., 2005; Barnyakov et al., 2000; Siudak et al., 2008). Further, with only a small loss of acceptance, the distances between the tracking planes could be enlarged in order to increase the sensitivity to deviations of charged particle tracks from a straight line.

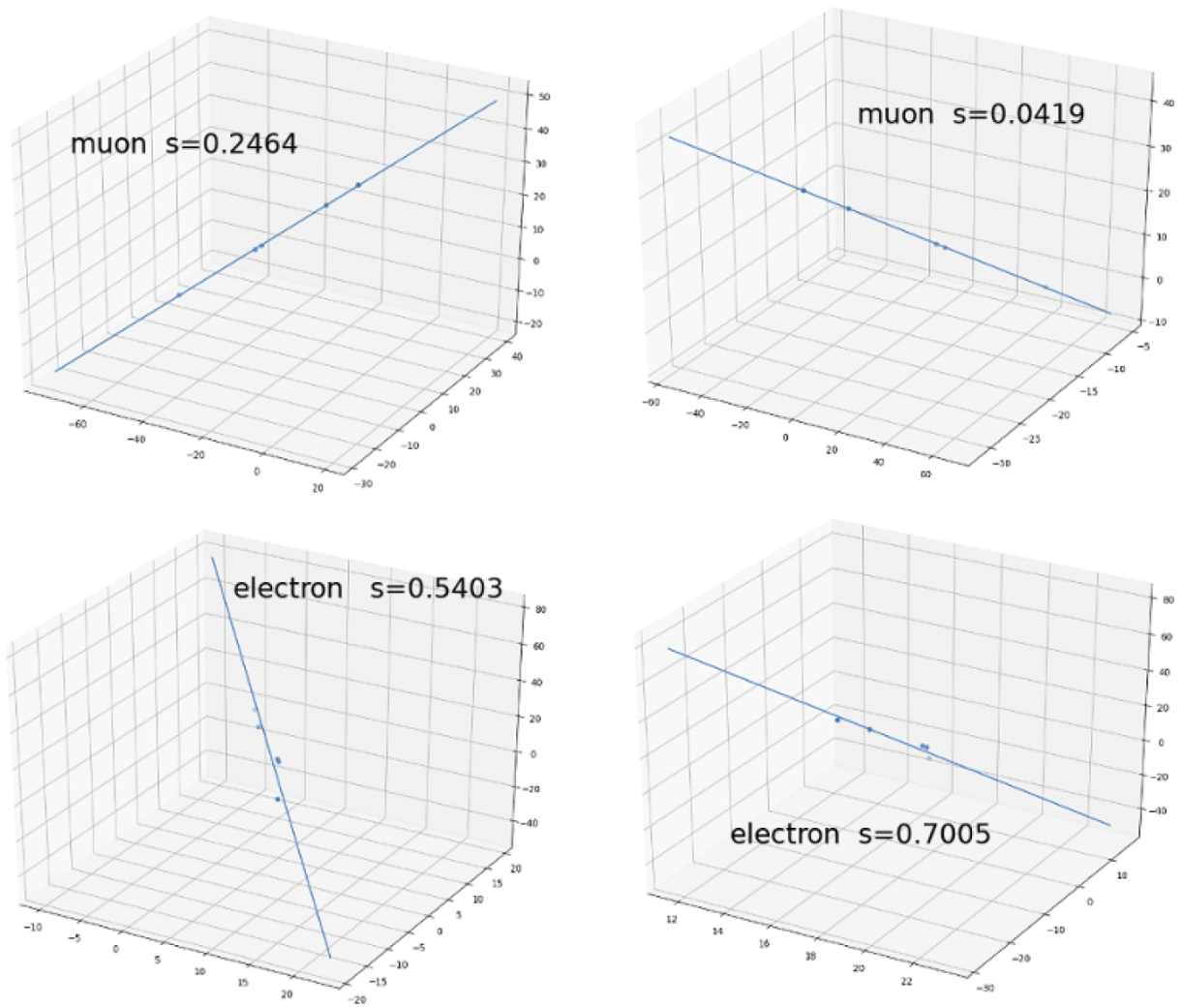


**Figure 28.** Example results from the implemented 3D line fitting (making use of SVD, Singular Value Decomposition) for two muon tracks on top and two electron type tracks on bottom.

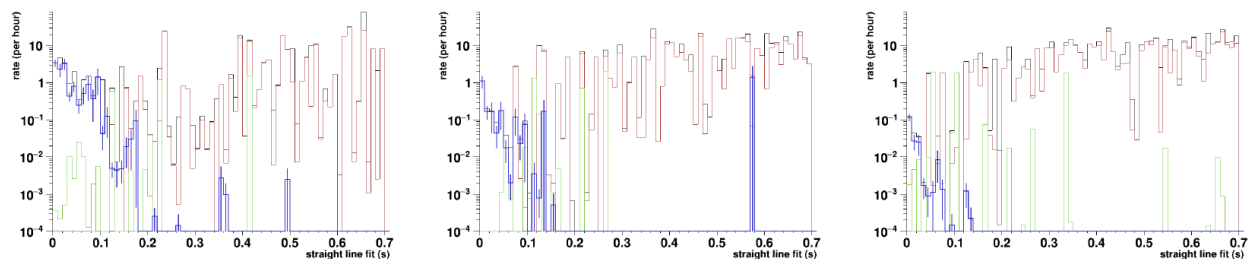


**Figure 29.** Deviation from a straight line for muon track candidates for asteroid models of  $2 \text{ g/cm}^3$  density and 20 m (**left**), 50 m (**middle**) and 100 m (**right**) diameter. All track candidates are shown by the black histogram while electron type (red), pion type (green) and muon track types (blue) are indicated. The statistical errors are shown for muon track candidates only.

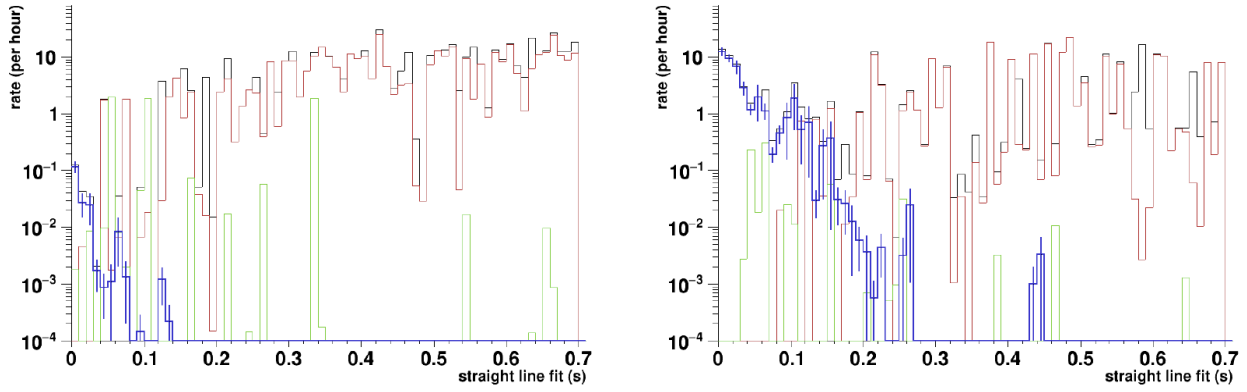


**Figure 30.** Deviation from a straight line for muon track candidates for asteroid models of 100 m diameter with 2.0 g/cm<sup>3</sup> density (**left**) and 0.5 g/cm<sup>3</sup> density (**right**). All track candidates are shown by the black histogram while electron type (red), pion type (green) and muon track types (blue) are indicated. The statistical errors are shown for muon track candidates only.

### Transmitted muon signal

Upward moving muon track candidates for directions within 30 degree of the surface normal were selected if every tracking plane recorded at least one but not more than two hits. At least 20 Cerenkov photons were required to reach the optical sensors. In Fig. 29 the quality spectrum of the 3D straight line fit for this subset of muon candidates is given as an example, with focus on likely straight tracks. Asteroid models with a density of 2 g/cm<sup>3</sup> and a size of 20 m, 50 m and 100 m diameter are considered from left to right. The rate of through-going muons decreases with increasing asteroid size forcing a more strict cut on the track quality in order to obtain a high fraction of muons in the selected event subset.

The predicted number of detected through-going muons for an asteroid of density 2.0 g/cm<sup>3</sup> is given in Table 2 with the selected track quality requirement. The number of found muon candidates is robust with respect to selected cut criteria, with the exception of the particle direction. Hence, the found rate is predominantly a function of how many muons are created by GCR with sufficient kinetic energy to traverse the asteroid.

**Table 3.** Predicted rate of detected through-going muons per day. The statistical uncertainty is in the order of 10%.

asteroid diameter	20 m	50 m	100 m
track quality cut	$s < 0.10$	$s < 0.05$	$s < 0.04$
signal rate (d <sup>-1</sup> )	500	42.6	4.88

### Asteroids of different size and density

As pointed out earlier, small low density asteroids of order 20 m diameter are not expected to feature a clear, easy to interpret, through-going muon signal. At the same time, for large high density asteroids of order 100 m diameter or more, the through-going muon signal rate will limit the feasibility of the proposed approach. This is apparent from Table 3 for asteroids of density 2 g/cm<sup>3</sup>.

A 100 m diameter asteroid of density  $0.5 \text{ g/cm}^3$  was simulated in order to assess the impact of low density on large asteroids. In Fig. 30 the straight track quality spectrum is shown on the right and compared to the earlier findings for a same size asteroid with a density of  $2.0 \text{ g/cm}^3$ .

A total of 863 through-going muons per day are conservatively predicted with a straight track quality requirement of  $s < 0.07$ . Even larger low density asteroids or comets could be investigated with the proposed approach.

## Mission concepts

Given the performance of the preliminary design for low-density targets, a mission to a comet, as highlighted in Figs. 17-19, would likely be feasible. This would involve landing on the comet to characterize its interior structure. The muon imaging system could monitor changes in the interior as the comet passes through perihelion with the goal of better understanding outgassing sources and mechanisms. Given the importance of comets to understanding the current state and evolution of the solar system, such a mission would return high-value science data.

Similarly, targeting small, near Earth asteroids would be of interest from the perspective of solar system science, resource utilization and planetary defense. It may be beneficial to deploy a hodoscope on a target that has already been the subject of extensive Earth- and spacecraft-based remote sensing. For example, direct measurements of Bennu's interior structure would complement surface observations by OSIRIS-Rex (Barnouin et al., 2019). Given Bennu's low bulk density (and high porosity), event rates would be sufficient to image portions of the asteroid's interior, albeit with lower precision and spatial resolution than for a comet. Data could be acquired from a lander or while flying in formation with the asteroid. In the latter case, the data could provide data suitable for 3D tomographic reconstruction of interior regions. Although not explored in this report, stand-off measurements may be feasible albeit with lower signal and higher background than surface measurements.

Before contemplating use of muography on any mission, additional steps are needed to fully prove and optimize the design of the muon imaging system. Candidate designs could be tested on balloon flights. The International Space Station (ISS) is already host to the Alpha Magnetic Spectrometer and perhaps the station could be used as an artificial "asteroid" to validate aspects of the instrument design. An instrument could be deployed on an ISS Express Logistics Carrier, which provides mechanical mount points, power, and command and data handling capabilities. Similarly, Lunar Orbital Platform – Gateway may be a desirable platform for testing the deep space performance of a prototype instrument.

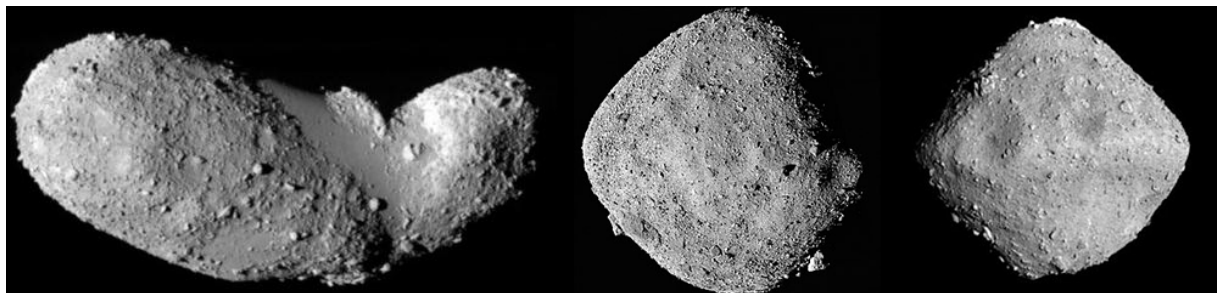


**Figure 31.** NEO Targets. (L) Itokawa,  $\sim 0.3 \text{ km}$ , target of Hayabusa 1, (C) Bennu,  $\sim 0.5 \text{ km}$ , target of OSIRIS-Rex, (R) Ryugu,  $\sim 0.9 \text{ km}$ , target of Hayabusa 2. The surfaces are strewn with boulders. (Image credits: JAXA and NASA).

## Spin-offs

Characterization of surface structures on airless bodies large and small, such as the rim of Stickney crater on Phobos or large boulders/features on the surface of asteroids, could be enabled by muography. Deployment of a muon imaging system on a lander or rover placed in the interior of Stickney crater was briefly considered for the JAXA/MMX mission. Measurements of the interior density structure of the rim would provide constraints on crater formation and the possible presence of interior water ice. The interior structure of large boulders on asteroids — up to ~50 m diameter on Bennu (Lauretta et al., 2019) — could provide information on aspects of the evolution and collisional history of rubble-pile asteroids.

The measurement of surface structures on Mars using the intense horizontal muon flux produced in the thin martian atmosphere was proposed by Kedar et al. (2013). Although this study acknowledged the requirement to reject secondary particles produced by galactic cosmic rays reaching the surface, a feasible instrument design for rejecting this background was not described. Given the mass of the electron scattering material used in our prototype imaging system (~500 kg), implementation on a rover platform may not be feasible. The atmosphere of Saturn's moon Titan is thicker and more extensive than that of Earth. Consequently, it may be possible to image surface geologic features on Titan with muons using compact instrumentation.

Another possible use of muography is the study of planetary caves. Numerous caves and collapse pits have been discovered on the Moon and Mars (e.g. Cushing et al., 2007; Kaku et al., 2017). The presence of these caves has implications in situ resource utilization, radiation shielding, and astrobiology (e.g. Boston et al., 2001). For example, lunar caves could cold trap water ice, which could serve as a potential resource and provide a record of the delivery of volatiles to the Moon. Mapping of cave structures and measurements of overburden may be possible using muography (Prettyman, Titus, et al., 2015). Deployment of an imaging system at depth would reduce background contributions, possibly resulting in a more compact system.

Of course, Earth applications of muography abound. With Planetary Science Institute internal funding, T. Prettyman has developed a compact muon overburden gauge which has undergone testing in caves in Hawaii, New Mexico and Arizona. Most recently, the gauge was used to survey of the Lava River Cave, an intact lava tube in Arizona. Preliminary results are shown in Fig. 32. Measurements were made at twelve locations spanning most of the length of the tube. Replicate measurements were made at selected locations the following day. The decreased overburden of the replicates may indicate a reduction in the water content of the rock above the cave following rainy weather. The possibility of using muons to monitor overburden is intriguing and connects back to the idea of monitoring the interior structure of comets. Further efforts to characterize Lava River and other caves is underway, with the aim of better characterizing their thermal environment and physical properties of the surrounding rock. The development of inexpensive and practical instrumentation for routine use by geologists continues.

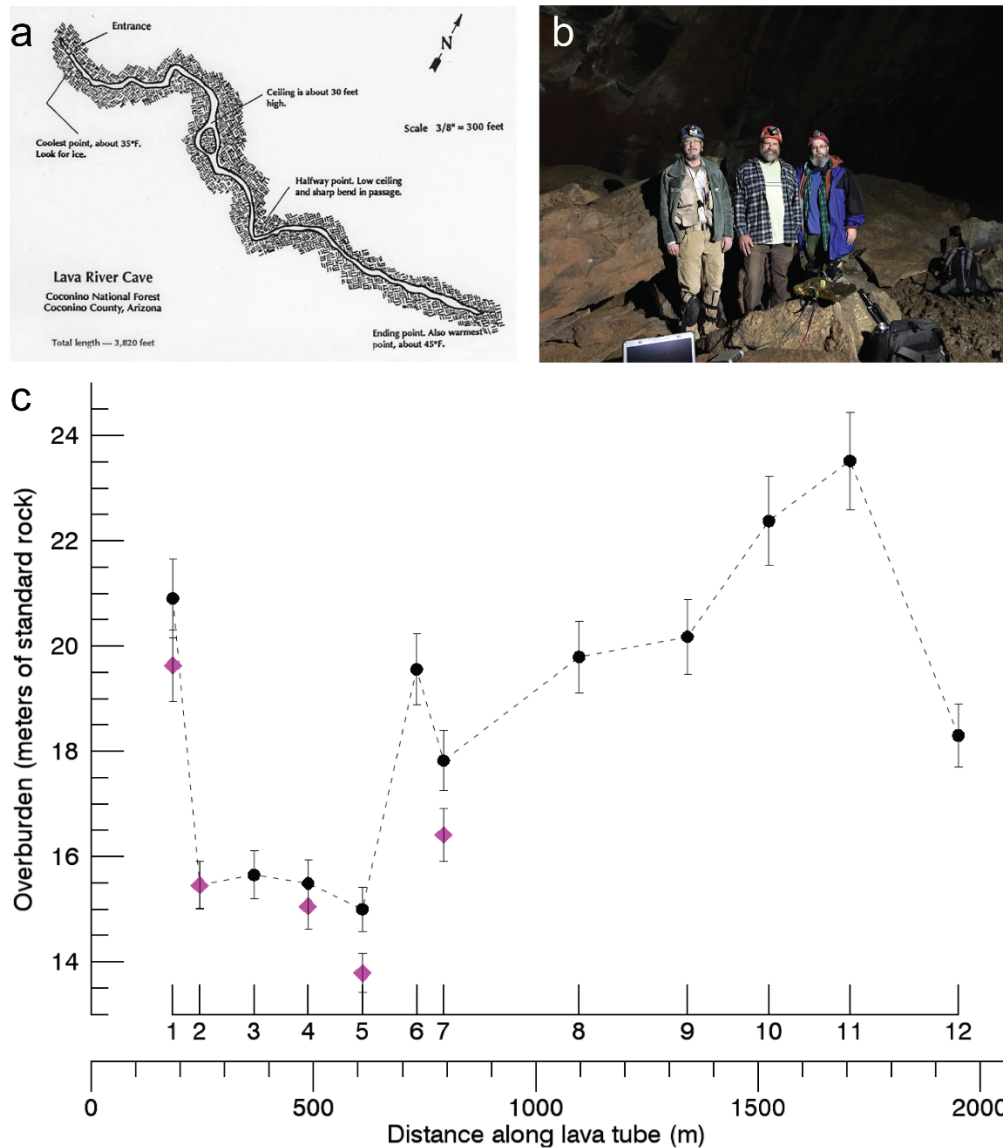


**Figure 32.** Muon overburden measurements in a lava tube. a) Map of the Lava River Cave (US Forest Service); b) Equipment and personnel at a measurement station within the cave (T. Titus, G. Cushing and T. Prettyman, left to right); c) Overburden measurements at 12 locations spanning most of the length of the cave acquired during the same day (black circles). The magenta symbols (diamonds) are replicate measurements made the following day.

## Conclusions and Next Steps

This study has demonstrated and numerically validated a feasible design for a muon imaging system that could be used to image the interior of small, airless bodies, including asteroids and comets. The design incorporates a hodoscope to detect and track transmitted muons; however, the imaging system also includes design features required to reject large backgrounds, enabling the through going muon signal to be measured. Use of an aerogel Cerenkov filter enables the suppression of a portion of particles produced by cosmic rays shower on the same side of the body as the detector. Electrons are rejected through the use of passive scattering materials placed around the imaging planes. The resulting imaging system is massive, 500 kg alone for the

materials used to shower the electrons; however, it is a starting point from which more compact designs could be realized. The technology, while state-of-the art is available and has been demonstrated for accelerator experiments.

The muon detection rate is expected to be very low compared to that encountered in Earth applications, which will limit the quality of structural information that can be extracted from the data (e.g. see Fig. 19). The event rate depends on the density of the near surface source region in which the muons are produced as well as the interior density and distance traversed. Nevertheless, muography could be applied to image interior regions within asteroids and comets less than a few hundred meters in size. For example, it may be possible to image portions of the interior of the Near Earth Asteroid Bennu, which has relatively low density ( $\sim 1 \text{ g/cm}^3$ ) and high porosity. Similarly, muography could be used to monitor the interior structure of a comet as it passes through perihelion, providing an entirely new view of cometary processes.

Next steps include optimization of the overall design of the muon imaging system and background suppression methods, with the goal of producing a more compact instrument. In addition, further experimental testing of components is needed. Benchtop tests with radiators, including aerogel and fused silica, using SiPMs and photomultiplier tubes were carried out by this project. Additional development and experimental testing of subcomponents for imaging, directionality and timing is needed to validate key aspects of the system design. Testing could be carried out with atmospheric muons and at accelerator facilities.

## **Acknowledgements**

The NIAC “Deep Mapping” project would not have been without the encouragement of Steve Koontz. Steve’s interest and enthusiasm in cosmic ray studies sparked a collaborative effort that led to improvements in radiation transport modeling capabilities for planetary applications. Participants in this project included A. Empl, M. C. Nolan, D. J. Lawrence, R. S. Miller, D. Mittlefehldt, L. S. Pinsky, T. H. Prettyman, B. D. Redell, and M. V. Sykes. T. H. Prettyman acknowledges his affiliation with the NASA Jet Propulsion Laboratory, which provided library resources needed to carry out this work. P. J. Boston suggested cave research as a possible spin-off of our project, including terrestrial and planetary caves. This led to the development of a prototype overburden gauge, which was tested in several caves, including lava tubes in Oahu (guided by N. Schorghofer), the Big Tubes in New Mexico (led by P. Boston and M. Spilde), and the Lava River Cave (T. Titus, G. Cushing, and T. Prettyman, participants).

## References

- Abt, I., Caldwell, A., Carissimo, C., Gooch, C., Kneißl, R., Langford, J., et al. (2017). The muon-induced neutron indirect detection EXperiment, MINIDEX. *Astroparticle Physics*, *90*, 1-13. doi:10.1016/j.astropartphys.2017.01.011
- Ahlen, S., Ambrosio, M., Antolini, R., Auriemma, G., Baldini, A., Bam, B., et al. (1993). Muon astronomy with the MACRO detector. *The Astronomical Journal*, *412*(1), 301-311.
- Allkofer, O. C., Carstensen, K., & Dau, W. D. (1971). The absolute cosmic ray muon spectrum at sea level. *Physics Letters B*, *36*(4), 425-427. doi:[https://doi.org/10.1016/0370-2693\(71\)90741-6](https://doi.org/10.1016/0370-2693(71)90741-6)
- Alvarez, L. W., Anderson, J. A., Bedwei, F. E., Burkhard, J., Fakhry, A., Girgis, A., et al. (1970). Search for Hidden Chambers in the Pyramids. *Science*, *167*(3919), 832-839. doi:10.1126/science.167.3919.832
- Ambrosio, M., Antolini, R., Auriemma, G., Baker, R., Baldini, A., Barbarino, G. C., et al. (1995). Vertical muon intensity measured with MACRO at the Gran Sasso laboratory. *Physical Review D*, *52*(7), 3793-3802. doi:10.1103/PhysRevD.52.3793
- Asaturyan, R., Ent, R., Fenker, H., Gaskell, D., Huber, G. M., Jones, M., et al. (2005). The aerogel threshold Cherenkov detector for the High Momentum Spectrometer in Hall C at Jefferson Lab. *Nuclear Instruments and Methods in Physics Research Section A: Accelerators, Spectrometers, Detectors and Associated Equipment*, *548*(3), 364-374. doi:10.1016/j.nima.2005.04.058
- Barnouin, O. S., Daly, M. G., Palmer, E. E., Gaskell, R. W., Weirich, J. R., Johnson, C. L., et al. (2019). Shape of (101955) Bennu indicative of a rubble pile with internal stiffness. *Nature Geoscience*, *12*(4), 247-252. doi:10.1038/s41561-019-0330-x
- Barnyakov, M. Y., Bobrovnikov, V. S., Buzykaev, A. R., Danilyuk, A. F., Ganzhur, S. F., Goldberg, I. I., et al. (2000). Aerogel Cherenkov counters for the KEDR detector. *Nuclear Instruments and Methods in Physics Research Section A: Accelerators, Spectrometers, Detectors and Associated Equipment*, *453*(1), 326-330. doi:10.1016/S0168-9002(00)00653-7
- Battistoni, G., Boehlen, T., Cerutti, F., Chin, P. W., Esposito, L. S., Fassò, A., et al. (2015). Overview of the FLUKA code. *Annals of Nuclear Energy*, *82*, 10-18. doi:10.1016/j.anucene.2014.11.007
- Battistoni, G., Ferrari, A., Montaruli, T., & Sala, P. R. (2002). Comparison of the FLUKA calculations with CAPRICE94 data on muons in atmosphere. *Astroparticle Physics*, *17*(4), 477-488. doi:10.1016/S0927-6505(01)00176-1
- Bellini, G., Benziger, J., Bick, D., Bonfini, G., Bravo, D., Avanzini, M. B., et al. (2013). Cosmogenic Backgrounds in Borexino at 3800 m water-equivalent depth. *Journal of Cosmology and Astroparticle Physics*, *2013*(08), 049-049. doi:10.1088/1475-7516/2013/08/049
- Binzel, R. P. (2014). Human spaceflight: Find asteroids to get to Mars. *Nature*, *514*, 559-561. doi:10.1038/514559a
- Blackmore, E. W., Stukel, M., Trinczek, M., Slayman, C., Wen, S., & Wong, R. (2015). Terrestrial Muon Flux Measurement at Low Energies for Soft Error Studies. *IEEE Transactions on Nuclear Science*, *62*(6), 2792-2796. doi:10.1109/TNS.2015.2498103
- Böhlen, T. T., Cerutti, F., Chin, M. P. W., Fassò, A., Ferrari, A., Ortega, P. G., et al. (2014). The FLUKA Code: Developments and Challenges for High Energy and Medical Applications. *Nuclear Data Sheets*, *120*, 211-214. doi:10.1016/j.nds.2014.07.049

- Böhm, M., Lehmann, A., Motz, S., & Uhlig, F. (2016). Fast SiPM Readout of the PANDA TOF Detector. *Journal of Instrumentation*, *11*(05), C05018-C05018. doi:10.1088/1748-0221/11/05/c05018
- Borovička, J., & Charvát, Z. (2009). Meteosat observation of the atmospheric entry of 2008 TC3 over Sudan and the associated dust cloud. *A&A*, *507*(2), 1015-1022. doi:10.1051/0004-6361/200912639
- Boston, P. J., Spilde, M. N., Northup, D. E., Melim, L. A., Soroka, D. S., Kleina, L. G., et al. (2001). Cave Biosignature Suites: Microbes, Minerals, and Mars. *Astrobiology*, *1*(1), 25-55. doi:10.1089/153110701750137413
- Bottke, W. F., Morbidelli, A., Jedicke, R., Petit, J.-M., Levison, H. F., Michel, P., & Metcalfe, T. S. (2002). Debaised Orbital and Absolute Magnitude Distribution of the Near-Earth Objects. *Icarus*, *156*(2), 399-433. doi:10.1006/icar.2001.6788
- Britt, D. T., Yeomans, D., Housen, K., & Consolmagno, G. (2002). Asteroid density, porosity, and structure. In A. C. W. Bottke, P. Paolicchi, and R. Binzel (Ed.), *Asteroids III* (pp. 485-500). Tucson: University of Arizona Press.
- Ciarletti, V., Levasseur-Regourd, A. C., Lasue, J., Statz, C., Plettemeier, D., Hérique, A., et al. (2015). CONSERT suggests a change in local properties of 67P/Churyumov-Gerasimenko's nucleus at depth. *Astronomy & Astrophysics*, *583*(A40). doi:10.1051/0004-6361/201526337
- Cushing, G. E., Titus, T. N., Wynne, J. J., & Christensen, P. R. (2007). THEMIS observes possible cave skylights on Mars. *Geophysical Research Letters*, *34*(17). doi:10.1029/2007GL030709
- Davis, D. R., Chapman, C. R., Greenberg, R., Weidenschilling, S. J., & Harris, A. W. (1979). Collisional evolution of asteroids: populations, rotations, and velocities. In T. Gehrels (Ed.), *Asteroids* (pp. 528-537). Tucson: University of Arizona Press.
- Du, Q., Abt, I., Empl, A., Gooch, C., Kneissl, R., Lin, S. T., et al. (2018). Direct measurement of neutrons induced in lead by cosmic muons at a shallow underground site. *Astroparticle Physics*, *102*, 12-24. doi:10.1016/j.astropartphys.2018.04.005
- Empl, A., Hungerford, E. V., Jasim, R., & Mosteiro, P. (2014). A Fluka study of underground cosmogenic neutron production. *Journal of Cosmology and Astroparticle Physics*, *2014*(08), 064-064. doi:10.1088/1475-7516/2014/08/064
- Ferrari, A., Sala, P. R., Fasso, A., & Ranft, J. (2005). FLUKA: A Multi-Particle Transport Code. *Technical Report CERN-2005-10, INFN/TC\_05/11, SLAC-R-773*.
- Gaisser, T. K. (1990). *Cosmic rays and particle physics*. Cambridge, UK: Cambridge University Press.
- Gauss, C. F. (1831). Besprechung des Buchs von L. A. Seeber: Untersuchungen über die eigenschaften der positivernären quadratischen formen. *Göttingische Gelehrte Anzeigen*, 1065.
- George, E. P. (1955). Cosmic rays measure overburden of tunnel. *Commonwealth Engineer*, 455-457.
- Goodrich, C. A., Hartmann, W. K., O'Brien, D. P., Weidenschilling, S. J., Wilson, L., Michel, P., & Jutzi, M. (2015). Origin and history of ureilitic material in the solar system: The view from asteroid 2008 TC3 and the Almahata Sitta meteorite. *Meteoritics & Planetary Science*, *50*(4), 782-809. doi:10.1111/maps.12401
- Groom, D. E., Mokhov, N. V., & Striganov, S. I. (2001). MUON STOPPING POWER AND RANGE TABLES 10 MeV–100 TeV. *Atomic Data and Nuclear Data Tables*, *78*(2), 183-356. doi:<https://doi.org/10.1006/adnd.2001.0861>
- Holsapple, K. A. (2007). Spin limits of Solar System bodies: From the small fast-rotators to 2003 EL61. *Icarus*, *187*(2), 500-509. doi:10.1016/j.icarus.2006.08.012

- Infantino, A., Blackmore, E. W., Brugger, M., Alía, R. G., Stukel, M., & Trinczek, M. (2016). FLUKA Monte Carlo assessment of the terrestrial muon flux at low energies and comparison against experimental measurements. *Nuclear Instruments and Methods in Physics Research Section A: Accelerators, Spectrometers, Detectors and Associated Equipment*, 838, 109-116. doi:10.1016/j.nima.2016.09.012
- Kaku, T., Haruyama, J., Miyake, W., Kumamoto, A., Ishiyama, K., Nishibori, T., et al. (2017). Detection of Intact Lava Tubes at Marius Hills on the Moon by SELENE (Kaguya) Lunar Radar Sounder. *Geophysical Research Letters*, 44(20), 10,155-110,161. doi:10.1002/2017GL074998
- Kedar, S., Tanaka, H. K. M., Naudet, C. J., Jones, C. E., Plaut, J. P., & Webb, F. H. (2013). Muon radiography for exploration of Mars geology. *Geosci. Instrum. Method. Data Syst.*, 2(1), 157-164. doi:10.5194/gi-2-157-2013
- Kofman, W., Herique, A., Barbin, Y., Barriot, J.-P., Ciarletti, V., Clifford, S., et al. (2015). Properties of the 67P/Churyumov-Gerasimenko interior revealed by CONSERT radar. *Science*, 349(6247), aab0639. doi:10.1126/science.aab0639
- Koontz, S., Reddell, B., & Boeder, P. (2010, 25-29 July 2011). *Calculating Spacecraft Single Event Environments with FLUKA: Investigating the Effects of Spacecraft Material Atomic Number on Secondary Particle Showers, Nuclear Reactions, and Linear Energy Transfer (LET) Spectra, Internal to Spacecraft Avionics Materials, at High Shielding Mass*. Paper presented at the 2011 IEEE Radiation Effects Data Workshop.
- Lauretta, D. S., DellaGiustina, D. N., Bennett, C. A., Golish, D. R., Becker, K. J., Balram-Knutson, S. S., et al. (2019). The unexpected surface of asteroid (101955) Bennu. *Nature*, 568(7750), 55-60. doi:10.1038/s41586-019-1033-6
- Mazanek, D. D., Brophy, J. R., & Merrill, R. G. (2013). *Asteroid Retrieval Mission Concept - Trailblazing Our Future in Space and Helping to Protect Us from Earth Impactors*. Retrieved from Flagstaff, AZ:
- McGaha, J. E., Jacques, C., & Pimentel, E. (2008). 2008-T50. In *Minor Planet Electronic Circular*: Minor Planet Center, Smithsonian Astrophysical Observatory, Cambridge, MA.
- Michel, P., & Richardson, D. C. (2013). Collision and gravitational reaccumulation: Possible formation mechanism of the asteroid Itokawa. *Astronomy & Astrophysics*, 554. doi:10.1051/0004-6361/201321657
- Morbidelli, A., Nesvorný, D., Bottke, W. F., Michel, P., Vokrouhlický, D., & Tanga, P. (2003). The shallow magnitude distribution of asteroid families. *Icarus*, 162(2), 328-336. doi:[https://doi.org/10.1016/S0019-1035\(02\)00076-3](https://doi.org/10.1016/S0019-1035(02)00076-3)
- Morishima, K., Kuno, M., Nishio, A., Kitagawa, N., Manabe, Y., Moto, M., et al. (2017). Discovery of a big void in Khufu's Pyramid by observation of cosmic-ray muons. *Nature*, 552, 386. doi:10.1038/nature24647
- Nakamura, A., & Fujiwara, A. (1991). Velocity distribution of fragments formed in a simulated collisional disruption. *Icarus*, 92(1), 132-146. doi:10.1016/0019-1035(91)90040-Z
- Nunes, D. C., & Phillips, R. J. (2006). Radar subsurface mapping of the polar layered deposits on Mars. *Journal of Geophysical Research*, 111(E06S21). doi:10.1029/2005JE002609
- O'Neill, P. M., Golge, S., & Slaba, T. C. (2015). Badhwar - O'Neill 2014 Galactic Cosmic Ray Flux Model Description. *NASA/TP-2015-218569*.
- Pätzold, M., Andert, T., Hahn, M., Asmar, S. W., Barriot, J. P., Bird, M. K., et al. (2016). A homogeneous nucleus for comet 67P/Churyumov-Gerasimenko from its gravity field. *Nature*, 530, 63. doi:10.1038/nature16535

- Phillips, R. J., Zuber, M. T., Smrekar, S. E., Mellon, M. T., Head, J. W., Tanaka, K. L., et al. (2008). Mars North Polar Deposits: Stratigraphy, Age, and Geodynamical Response. *Science*, 320(5880), 1182. doi:10.1126/science.1157546
- Prettyman, T. H., Koontz, S., Pinsky, L., Empl, A., Mittlefehldt, D. W., Reddell, B., & Sykes, M. (2014). *Deep mapping of small solar system bodies with galactic cosmic ray secondary particle showers*. Retrieved from 2013 NIAC Phase I Project Reports: [https://www.nasa.gov/sites/default/files/files/Prettyman\\_2013\\_PhI\\_MuonDeepMapping.pdf](https://www.nasa.gov/sites/default/files/files/Prettyman_2013_PhI_MuonDeepMapping.pdf)
- Prettyman, T. H., Titus, T. N., Boston, P. J., Koontz, S., & Miller, R. S. (2015). Mapping overburden and cave networks with muons. *2nd International Planetary Caves Conference*, Abstract #9030.
- Prettyman, T. H., Yamashita, N., Reedy, R. C., McSween, H. Y., Mittlefehldt, D. W., Hendricks, J. S., & Toplis, M. J. (2015). Concentrations of potassium and thorium within Vesta's regolith. *Icarus*, 259, 39-52. doi:10.1016/j.icarus.2015.05.035
- Roesler, S., Heinrich, W., & Schraube, H. (2002). Monte Carlo Calculation of the Radiation Field at Aircraft Altitudes. *Radiation Protection Dosimetry*, 98(4), 367-388. doi:10.1093/oxfordjournals.rpd.a006728
- Sánchez, P., & Scheeres, D. J. (2014). The strength of regolith and rubble pile asteroids. *Meteoritics & Planetary Science*, 49(5), 788-811. doi:10.1111/maps.12293
- Sava, P., & Asphaug, E. (2018). 3D radar wavefield tomography of comet interiors. *Advances in Space Research*, 61(8), 2198-2213. doi:<https://doi.org/10.1016/j.asr.2018.01.040>
- Scheeres, D. J., Hartzell, C. M., Sánchez, P., & Swift, M. (2010). Scaling forces to asteroid surfaces: The role of cohesion. *Icarus*, 210(2), 968-984. doi:10.1016/j.icarus.2010.07.009
- Shaddad, M. H., Jenniskens, P., Numan, D., Kudoda, A. M., Elsir, S., Riyad, I. F., et al. (2010). The recovery of asteroid 2008 TC3. *Meteoritics & Planetary Science*, 45(10-11), 1557-1589. doi:10.1111/j.1945-5100.2010.01116.x
- Siudak, R., Budzanowski, A., Chatterjee, A., Clement, H., Dorochkevitch, E., Ernst, J., et al. (2008). A threshold Cherenkov detector for K<sup>+</sup>/π<sup>+</sup> separation using silica aerogel. *Nuclear Instruments and Methods in Physics Research Section A: Accelerators, Spectrometers, Detectors and Associated Equipment*, 596(3), 311-316. doi:10.1016/j.nima.2008.08.129
- Stokes, G. H., Barbee, B. W., Bottke, W. F., Chesley, S. R., & Yeomans, D. K. (2017). Update to Determine the Feasibility of Enhancing the Search and Characterization of Neos Report of the Near-Earth Object Science Definition Team. Retrieved from [https://cneos.jpl.nasa.gov/doc/2017\\_neo\\_sdt\\_final\\_e-version.pdf](https://cneos.jpl.nasa.gov/doc/2017_neo_sdt_final_e-version.pdf)
- Sykes, M. V., Grün, E., Reach, W. T., & Jenniskens, P. (2004). The interplanetary dust complex and comets. In *Comets II* (pp. 677-693): University of Arizona Press.
- Sykes, M. V., & Walker, R. G. (1992). Cometary dust trails: I. Survey. *Icarus*, 95(2), 180-210. doi:10.1016/0019-1035(92)90037-8
- Tanaka Hiroyuki, K. M. (2019). Japanese volcanoes visualized with muography. *Philosophical Transactions of the Royal Society A: Mathematical, Physical and Engineering Sciences*, 377(2137), 20180142. doi:10.1098/rsta.2018.0142
- Tanaka, H. K. M. (2015). Muographic mapping of the subsurface density structures in Miura, Boso and Izu peninsulas, Japan. *Scientific Reports*, 5, 8305. Article. doi:10.1038/srep08305
- Tanaka, H. K. M., Kusagaya, T., & Shinohara, H. (2014). Radiographic visualization of magma dynamics in an erupting volcano. *Nature Communications*, 5, 3381. Article. doi:10.1038/ncomms4381  
<https://www.nature.com/articles/ncomms4381#supplementary-information>
- Tanaka, H. K. M., Nakano, T., Takahashi, S., Yoshida, J., Takeo, M., Oikawa, J., et al. (2007). High resolution imaging in the inhomogeneous crust with cosmic-ray muon radiography: The

- density structure below the volcanic crater floor of Mt. Asama, Japan. *Earth and Planetary Science Letters*, 263(1), 104-113. doi:<https://doi.org/10.1016/j.epsl.2007.09.001>
- Tanaka, H. K. M., Uchida, T., Tanaka, M., Shinohara, H., & Taira, H. (2009). Cosmic-ray muon imaging of magma in a conduit: Degassing process of Satsuma-Iwojima Volcano, Japan. *Geophysical Research Letters*, 36(1). doi:10.1029/2008GL036451
- Tanaka, H. K. M., Uchida, T., Tanaka, M., Shinohara, H., & Taira, H. (2010). Development of a portable assembly-type cosmic-ray muon module for measuring the density structure of a column of magma. *Earth, Planets and Space*, 62(2), 119-129. doi:10.5047/eps.2009.06.003
- Thomas, P. C., & Robinson, M. S. (2005). Seismic resurfacing by a single impact on the asteroid 433 Eros. *Nature*, 436(7049), 366-369. doi:10.1038/nature03855
- Tioukov, V., Alexandrov, A., Bozza, C., Consiglio, L., D'Ambrosio, N., De Lellis, G., et al. (2019). First muography of Stromboli volcano. *Scientific Reports*, 9(1), 6695. doi:10.1038/s41598-019-43131-8
- Torquato, S., & Stillinger, F. H. (2007). Toward the jamming threshold of sphere packings: Tunneled crystals. *Journal of Applied Physics*, 102(9), 093511. doi:10.1063/1.2802184
- Trovati, S., Ballarini, F., Battistoni, G., Cerutti, F., Fassò, A., Ferrari, A., et al. (2006). Human exposure to space radiation: role of primary and secondary particles. *Radiation Protection Dosimetry*, 122(1-4), 362-366. doi:10.1093/rpd/ncl438
- Welten, K. C., Meier, M. M. M., Caffee, M. W., Nishiizumi, K., Wieler, R., Jenniskens, P., & Shaddad, M. H. (2010). Cosmogenic nuclides in Almahata Sitta ureilites: Cosmic-ray exposure age, preatmospheric mass, and bulk density of asteroid 2008 TC3. *Meteoritics & Planetary Science*, 45(10-11), 1728-1742. doi:10.1111/j.1945-5100.2010.01106.x